Article:
Wright, T.J., Houseman, G.A., Fang, J. et al. (2026) High-resolution geodetic velocities reveal role of weak faults in deformation of Tibetan Plateau. Science, 391 (6784). pp. 499-503. ISSN: 0036-8075

https://doi.org/10.1126/science.adi3552

High-resolution geodetic velocities reveal role of weak faults in deformation of Tibetan Plateau

Authors: T.J. Wright[1]*, G.A. Houseman[2,1], J. Fang[1]*, Y. Maghsoudi[3], A.J. Hooper[1], J.R. Elliott[1], L. Evans[4], M. Lazecky[1], Q. Ou[5], B.E. Parsons[6], J.C. Rollins[7], L. Shen[8], H. Wang[9], D. Wang[1]

Affiliations:

[1] COMET, School of Earth and Environment, University of Leeds, Leeds, UK
[2] State Key Laboratory of Deep Earth Exploration and Imaging, China University of Geosciences, Beijing, China
[3]COMET, Department of Earth and Environmental Sciences, University of Exeter, Penryn, UK
[4] School of Earth, Atmosphere & Environment, Monash University, Clayton, VIC, Australia
[5] COMET, School of GeoSciences, University of Edinburgh, Drummond, Edinburgh, UK
[6] COMET, Department of Earth Sciences, University of Oxford; Oxford, UK
[7] GNS Science, Lower Hutt, New Zealand
[8] Lamont-Doherty Earth Observatory, Columbia University, New York, USA
[9] College of Natural Resources and Environment, South China Agricultural University, Guangzhou, China

*Corresponding authors. Email: t.j.wright@leeds.ac.uk; j.fang@leeds.ac.uk

High-resolution geodetic velocities reveal role of weak faults in deformation of Tibetan Plateau

Authors: T.J. Wright[1]*, G.A. Houseman[2,1], J. Fang[1]*, Y. Maghsoudi[3], A.J. Hooper[1], J.R. Elliott[1], L. Evans[4], M. Lazecky[1], Q. Ou[5], B.E. Parsons[6], J.C. Rollins[7], L. Shen[8], H. Wang[9], D. Wang[1]

Affiliations:

[1] COMET, School of Earth and Environment, University of Leeds, Leeds, UK
[2] State Key Laboratory of Deep Earth Exploration and Imaging, China University of Geosciences, Beijing, China
[3]COMET, Department of Earth and Environmental Sciences, University of Exeter, Penryn, UK
[4] School of Earth, Atmosphere & Environment, Monash University, Clayton, VIC, Australia
[5] COMET, School of GeoSciences, University of Edinburgh, Drummond, Edinburgh, UK
[6] COMET, Department of Earth Sciences, University of Oxford; Oxford, UK
[7] GNS Science, Lower Hutt, New Zealand
[8] Lamont-Doherty Earth Observatory, Columbia University, New York, USA
[9] College of Natural Resources and Environment, South China Agricultural University, Guangzhou, China

*Corresponding authors. Email: t.j.wright@leeds.ac.uk; j.fang@leeds.ac.uk

Abstract:

Understanding the key mechanisms that control the tectonic deformation of the continents remains a fundamental challenge in geodynamics. We present a high-resolution geodetic velocity field of the Tibetan Plateau, which shows that a few major strike-slip fault systems separate regions of more uniformly distributed deformation. We suggest that focused strain on major fault systems is enabled by relatively low-viscosity ductile shear zones extending through the lithosphere beneath the seismically active fault planes. Simple model calculations show that high slip rates on the Kunlun Fault enable east-west extension to be distributed broadly across the relatively weak southern and central Tibetan Plateau. Activation of the Kunlun fault in the Miocene at the same time as onset of rifting in the north–south grabens suggests a causal relationship.

One-Sentence Summary: New satellite data reveal how major fault systems influence the tectonic deformation of the Tibetan Plateau.

Collision of the Indian tectonic plate with Eurasia over the last ca. 55 Ma has created an extensive region of deforming crust that extends from the Himalayas in the south, through the Tibetan Plateau, and into Central Asia (*1,2*). Continents deform through a combination of continuous distributed deformation and focused strain on lithospheric-scale faults (*3-6*). Much of the small-scale seismic activity in regions of continental deformation can be explained by a relatively superficial crustal layer comprised of minor crustal blocks that are carried along by a ductile substrate (*7*). However, it has long been clear that relatively few major fault zones (*8*) have a significant effect on continental deformation and seismic hazard. The importance of these major fault zones in controlling the overall deformation field has been difficult to assess given the limited spatial resolution of available geodetic displacement maps. We here document a large-scale compilation of geodetic data for the Tibetan Plateau that quantifies how the

deformation field of the India–Eurasia continental collision is controlled by a combination of both long-wavelength continuous deformation and strain focused on a few major fault systems. Better models of how the continents deform are important for seismic hazard assessment as they determine the degree to which earthquakes are focused on closely monitored major faults or occur on minor faults, which are often of unknown significance (*9*). Dynamical models that incorporate focused deformation on the major fault systems using the concept of a fault resistance coefficient (*10*) provide new quantitative constraints on the deep ductile shear zones inferred from diverse lines of evidence (*11*), and evident now in offset structure in the mantle beneath crustal faults (e.g. *12*).

The Tibetan Plateau is the world's largest region of continental deformation and has long been the testing ground for models of continental tectonics (e.g., *13-16*). As geodetic observations, particularly from Global Navigation Satellite Systems (GNSS), have improved (e.g., *17*), models have been refined, with recent kinematic models resolving elastic deformation within blocks and fault-slip rates on their boundaries (e.g., *18*). However, ground-based GNSS observations remain relatively sparse in parts of the Tibetan plateau (e.g., *19*). With 10 years of observation from the Sentinel-1 radar constellation (*20*) and, as a result of advances in Interferometric Synthetic Aperture Radar (InSAR) processing (*21, 22*), we compiled near-complete maps of present-day displacement and strain rates across the Tibetan Plateau. These maps provide the level of detail required to quantify the relative importance of continuous ductile deformation and localized discontinuous displacement on the major fault systems. The plateau is largely the consequence of crustal thickening due to north–south convergence but is now extending in an approximately east–west direction (*23*). The extension is caused by excess gravitational potential energy of the plateau (*24*); our data and models show the critical role of major fault systems in controlling the spatial distribution and rate of both north-south shortening and east-west extension.

Surface velocities and strain rates

To map surface velocities at high resolution, we first produced a network of short-baseline Sentinel-1 interferograms in 127 ascending and 114 descending frames covering the Tibetan Plateau (Fig. S1) using the COMET-LiCSAR system (*21*), spanning 2016 to 2024. More details of our approach are given in the Supplementary Materials (*SM*). We used the LiCSBAS algorithm (*22,25*) to compute average line-of-sight surface velocities for each frame (*SM.1-2*). To avoid contamination, we removed signals from coseismic deformation for earthquakes larger than M_w 6 before calculating the average velocities (*SM.3*). Line-of-sight velocities for each frame were initially independently referenced. Then we used a compilation of GNSS velocities and levelling data (*SM.4;* Fig. S2) to jointly invert for reference frame adjustment parameters and smooth 3D velocities on a ~0.2° triangular mesh (Fig. S1), following (*26,27*) (*SM.5*; Fig. S3), hereafter referred to as the *coarse* velocity model. The inverted reference frame parameters allowed us to derive mosaics of ascending and descending line-of-sight velocities tied to the Eurasian reference frame (Fig. S4). Following (*28*), we used the Eurasian line-of-sight mosaics to solve for east–west (Fig. 1) and vertical (Figs. 2B, S5) velocities at 1 km resolution in areas where both ascending and descending data exist, using the north–south velocities from the *coarse* velocity model (Fig. 2A) as a constraint. The spatial gradients of the horizontal velocities were used to derive horizontal strain rates and rotation rates in a spherical coordinate system (*SM.5*; Figs. 2, S6-8). Uncertainties in the velocities are generally less than 2 mm/yr, as described in (*SM.6;* Figs. S3, S9-12).

The horizontal velocity and strain-rate fields (Figs. 1, 2) reveal how the Tibetan Plateau is deforming in response to northward motion of the Indian plate. The broad-scale deformation pattern is consistent with previous studies (e.g. *19, 29*) that show plateau shortening in a direction parallel to the plate-motion convergence vector of India relative to Eurasia and also extending perpendicular to this direction (Fig. 1). South of the Kunlun fault, extension outpaces convergence, resulting in dilatation and likely crustal thinning (Fig. 2), consistent with inference from earthquake mechanisms (*23*).

The vast majority (95%) of inverted vertical velocities (Fig. 2) in the plateau fall in the range +/- 5 mm/yr; this range is only slightly larger than our estimate of uncertainty in the vertical velocities ($2\sigma \approx 3$ mm/yr; Fig. S11). Short wavelength components of the vertical velocities are in some cases correlated with topography and can be attributed to surficial processes including loss of permafrost, hydrological changes, and anthropogenic activity (*30*), as well as potential contamination from phase biases (*31*). Longer wavelength vertical signals are largely controlled by GNSS and levelling observations (Fig. S13); these are generally larger than can be explained by horizontal lithospheric tectonics. For example, the dilating region south of the Kunlun fault (outlined in Fig. 2D) has an average rate of dilatation of 6 nanostrain/yr; assuming isostatic balance operates on long wavelengths, we obtain a subsidence rate of < 0.1 mm/yr. The disconnect between horizontal tectonics and observed vertical motions is also evidenced by the lack of correlation between vertical rates and the dilatation field (Fig. 2). An exception is where we see uplift associated with interseismic elastic deformation on Himalayan thrust systems (*32*). Vertical motions likely arise primarily from permafrost (*30*), hydrological loading (*33*), glacial isostatic adjustment (34), and deeper mantle processes (*35*).

Compared to GNSS-derived strains (Fig. S14), the inclusion of InSAR data in our velocity field sharpens the spatial resolution of deformation observations, particularly in the interior of the plateau (Figs. 2, S6-8), where the gradients in east–west velocities (well resolved by InSAR) are highest. The strain-rate field clearly demonstrates that the highest strain rates in the plateau interior are focused on major strike-slip fault systems: the Altyn Tagh, Kunlun, Haiyuan, and Xian Shui He faults (Fig. 2). Velocity profiles not crossing these major fault systems do not in general show significant strain concentrations associated with minor mapped faults (Fig. 1). The major fault systems separate regions of relatively low strain rate; however, the second invariant of the strain rate tensor in the plateau interior (region shown on Fig. 2D) is still relatively high, with a median value of 24 nanostrain/yr, compared to typical values of 2–3 nanostrain/yr in stable continental regions (*36*) and significantly higher than the 9 nanostrain/yr we estimate in the Sichuan basin (*SM.6*). The eastward displacement of the plateau is associated with diffuse east–west extension in the south–central Tibetan Plateau, and outward flow and rotation (Fig. S7) around the eastern Himalayan syntaxis (Fig. 1). In the northeastern Tibetan Plateau, north–south contraction implies crustal thickening and active topographic growth (*30,37*).

Several of the fault systems within the plateau have been affected by earthquakes in the 20-year period before the Sentinel-1 observations, including the 1997 M_w 7.4 Manyi and 2001 M_w 7.8 Kokoxili earthquakes, on the Kunlun Fault and its westward extension, and the 2008 M_w 7.2 and 2014 M_w 6.9 Yutian earthquakes, associated with the westward termination of the Altyn Tagh fault (Fig. 1). We observe elevated post-seismic strain rates where the faults slipped in those recent events (Fig. 2). These include both localized shear strains and dilatations, with the Yutian Fault showing apparent areal dilation and the Kokoxili/Manyi ruptures showing apparent contraction. It is important to note that high strain rates occur elsewhere on major fault systems

in locations where there were no recent earthquakes. For example, there is no known historic rupture of the Kunlun fault east of 100°E (*38*), but shear strain rates remain high on the fault. We interpret the high-strain rates observed away from recent ruptures as being characteristic of the inter-seismic part of the earthquake cycle (*39*). Previous studies of the earthquake deformation cycle on other major strike-slip fault systems have shown that steady, high inter-seismic strain rates are reached following a few decades of elevated post-seismic strain rates (*40-42*).

Geodynamic modelling

We developed a quantitative dynamical model to explain the observed deformation field. We adapted the thin viscous sheet model (*13*) by including fault-like discontinuities at pre-defined locations and solved for the displacement-rate field represented on a spherical shell in a regional domain that covers the Tibetan Plateau and most of the Central Asia collision zone (*10,43;* Fig. 3A). Model faults were defined based on zones of localized shear (Fig. 2C). Thus, we included a simplified representation of the Kunlun, Haiyuan, Altyn Tagh, Sagaing, and Xian Shui He faults. In the model, horizontal displacement rates are independent of depth, and stresses were averaged across the thickness of the lithosphere, so that we obtained a two-dimensional representation of the instantaneous horizontal velocity field from which we derived the strain-rate distribution. We assumed that the thin viscous shell deforms according to a depth-averaged non-linear constitutive law,

$$\tau_{ij} = B\dot{E}^{(1-n)/n}\dot{\varepsilon}_{ij}, \text{ where } \dot{E} = \sqrt{\dot{\varepsilon}_{ij}\dot{\varepsilon}_{ij}} \quad (1)$$

in which deviatoric stress τ is a function of strain-rate, $\dot{\varepsilon}$, and depth-averaged viscosity coefficient, B. Eq (1) is a frame-invariant statement of the simplified idea that strain-rate varies as the nth power of depth-averaged deviatoric stress. We assumed $n = 3$, a typical value for olivine (*44*), which comprises the major mineral of the mantle lithosphere, but is also representative of the vertically averaged stress vs strain-rate relation (*45*). In our simplified depth-averaged model of the lithosphere at continental scale, we represented each major fault as a discontinuity in which the horizontal traction component acting on the fault plane (tangential σ_t or normal σ_n) is proportional to the discontinuity in displacement rate across the fault (tangential Δu_t, or normal Δu_n), considered an average rate over multiple earthquake cycles:

$$\sigma_t = f_t \Delta u_t; \sigma_n = f_n \Delta u_n \quad (2)$$

The proportionality constants (fault-resistance coefficients f_t, f_n) similarly represent a depth-average of the resistance to localized relative displacement in strike-parallel (or strike-perpendicular) direction. The fault resistance coefficient is a convenient way to characterize the behavior of an active fault zone system without prejudging its value, or its variability, on a particular fault.

We obtained apparent values of f on specific faults in this calculation by adjusting f until there was a good match to the geodetic velocity field. Thus, with this relatively simple model we could examine the effect of allowing localized shear strain on lithospheric-scale fault systems within a continuously deforming region.

Boundary conditions on the external edges of the model domain (Fig. 3A; S15) simulate the relative plate rotations of India (*46*) and the Yangtze and Amur plates (*47*) with respect to Eurasia. The force balance includes the effect of spatially variable gravitational potential energy,

here calculated assuming local isostatic balance of topography from ETOPO1 (*48*) smoothed with a 20-km-wide Gaussian filter.

We assumed that the viscosity coefficient B in Eq. (1) can vary spatially (Fig. 3A). The reference value of B that applies in the far-field (B_0) is constrained by the Argand number, Ar, which scales the relative magnitude of viscous stress in the collision zone to the stress differences caused by variations in gravitational potential energy (*13*). In regions representing India, and the Tarim, Sichuan and Alashan-Ordos basins, we set $B = 10B_0$ so the regions would behave like nearly rigid blocks within the deforming domain (Fig. S15). We constrained the various free parameters (Ar, regional B values, and fault resistance coefficients f) by extensive numerical experimentation in which we minimized the misfit between observed and model geodetic velocities (*10*). From these experiments we determined that the Tibetan Plateau and Tian Shan regions have a lesser viscosity coefficient ($0.3B_0$) and south-central Tibet is required to be even weaker ($0.1B_0$; Fig. S15). Although the requirement for a low viscosity plateau region (*10*) is necessary to fit the geodetic strain-rate field, it is consistent with the history of extensive volcanism and magmatism across the plateau (*49*, *50*) and geophysical observations of low shear-wave velocities and high electrical conductivity in the Tibetan upper crust (*51*), which suggest extensive zones of partial melt and hydrothermal activity.

Implications for fault strength

Model calculations show that changes to f on a given active fault change the velocity field over distances comparable to the length of the fault. The best fit to observed present-day velocity field requires different f values for different faults, but in general the major fault systems are relatively weak (Fig. S15). When f is small on east-west oriented fault systems like the Kunlun the result is significantly increased eastward velocities south of the fault (Figs. 1, 3A,B). Transient postseismic deformation can also impact estimates of f. For example, the velocity change across the western end of the Kunlun Fault, which was impacted by the Kokoxili and Manyi earthquakes, is best matched using $f = 0$; whereas the unimpacted eastern half of the fault requires a higher, but still small, value of f (i.e., dimensionless $f' = 0.5$, with scaling defined in (*10*); Fig. S16-17).

To illustrate why the Kunlun fault system has such a large impact on east–west extension over most of south-central Tibet, we show (Figs. 3C,D,E, *SM.7*, S18,S19) a simplified mechanical model that reduces the problem to its essential elements: a rectangular region of north–south extent W and viscosity $\eta = B_0/2$ (with n=1) bounded to the north by a major strike-slip fault and driven into extension by a contrast in gravitational potential energy on its eastern boundary. Solutions obtained for this simplified model show the primary role of f that applies to the northern boundary of the rectangular domain (Figs. 3D,E, S18, S19), representing the Kunlun Fault. For $f = \infty$ (Fig. 3D), equivalent to a rigid northern boundary, solutions imply that extension is locally restricted to near the eastern boundary. By contrast, in solutions with a dimensionless fault resistance parameter $f' = 0.5$ or less (with $f' = \frac{Wf}{\eta}$ in the simplified model), representing a weak fault, the extensional strain-rate field spans most of the region (Fig. 3C; S18). The simple model and related analytical solutions explain the length scales of the systematic northward and eastward increase in the east component of geodetic velocities (*SM.8*).

Comparing observed north–south profiles of the eastward velocities (e.g. Figs. 1C, 3F) with predictions of the simplified model (Fig. 3, S19) shows that the apparent value of f' on the Kunlun fault system must be less than ~0.5. For an effective viscosity of the lithosphere in the

plateau of $\eta \approx 10^{22}$ Pa s (*10*) and a slip rate of 10 mm/yr, we obtained a depth-averaged effective shear stress on the fault system that is about 2 MPa (*SM.7*). A stress drop of around 4 MPa was estimated for the 2001 Kokoxili earthquake on the Kunlun Fault (*52*), consistent with the global median of stress drops on continental transform-fault earthquakes of 3.5 MPa (*53*). Even if earthquakes on the Kunlun fault release all the stress in the seismogenic crust, average stress levels in the inferred ductile shear-zone beneath appear to be significantly less than those in the seismogenic crust.

If we assume the ductile shear zone supports similar stresses to the seismogenic fault, and the ductile shear zone is on average about 10 km wide, consistent with observations summarized in *(6)*, then the apparent effective viscosity of the shear zone is about $\sim 6 \times 10^{19}$ Pa s (*SM.7*); narrower shear zones require even lower viscosities. The low-viscosity shear zones required beneath the major active faults can arise due to localization mechanisms including shear heating (e.g. *54,55*), grain size reduction (e.g. *56*), fabric development (e.g. *57*) and fluid fluxing (e.g. *58, 59).* For weakening caused by thermal feedback, an apparent reduction in effective viscosity of the shear zone by a factor of ~250 would imply a localized temperature increase (for olivine) of ~200ºC. It is likely that weakening processes are only developed and sustained for those faults with a stable geometry that can accrue significant (tens of km) displacements. Among possible schematic rheological models of the lithosphere considered by Burgmann and Dresen (*6*), our understanding of the Tibetan strain rate field is most consistent with their "banana-split" model, in which the low strength of major fault zones limits the magnitude of lithospheric stress.

Relatively few of the Tibetan fault systems exhibit high strain rates, and there is significant variation in their apparent fault resistance, *f*. Most of the known faults on the plateau (Fig. 1) are not associated with high strain rates (Fig. 2). What mechanisms allow particular lithospheric-scale fault systems, such as the Kunlun, to be activated and sustained? One explanation is that active fault systems initially develop along pre-existing suture zones that are favorably oriented with respect to the stress field, e.g., the Kunlun fault and the Anyimaqen-Kunlun-Muztagh suture (*1*). Another possibility is that deep shear zones develop along boundaries between regions of differing rheological strength, e.g., the Altyn Tagh fault along the southeast margin of the Tarim Basin (*60*). Once established, the weakened fault systems have a major effect on the distribution of velocities and strain rates across the entire plateau, and we might expect the apparent *f* value to decrease in time as fault systems mature, increasing their offset and length. For example, our models show that although extension in southern and central Tibet is driven by the contrast in gravitational potential energy on the plateau's southeastern margin, the rates of extension and their spatial extent are strongly enhanced by the relatively weak Kunlun fault system. We suggest there is a causal link between mid-Miocene activation of the Kunlun fault (*61,62*) and the apparently synchronous onset of east–west extension on a series of rifts in south-central Tibet (*63,64*).

References

1. A. Yin, T. M. Harrison, Geologic evolution of the Himalayan-Tibetan orogen, *Annu. Rev. Earth Planet. Sci.* **28**, 211–80 (2000).

2. P. England, P. Molnar, Active deformation of Asia: From kinematics to dynamics. *Science* **278**, 647-650 (1997).

3. J. P. Avouac, P. Tapponnier, Kinematic model of active deformation in central Asia. *Geophys. Res. Lett.* **20**, 895-898 (1993).

4. W. Thatcher, Microplate model for the present-day deformation of Tibet, *J. Geophys. Res.* **112**, B01401 (2007) doi:10.1029/2005JB004244

5. L. Wang, S. Barbot, Three-dimensional kinematics of the India-Eurasia collision, *Commun. Earth Environ.* **4**:164 (2023). doi:10.1038/s43247-023-00815-4

6. R. Bürgmann and G. Dresen, Rheology of the Lower Crust and Upper Mantle: Evidence from Rock Mechanics, Geodesy, and Field Observations, *Annu. Rev. Earth Planet. Sci.* **36**, 531–567 (2008).

7. S. Bourne, P. England, B. Parsons, The motion of crustal blocks driven by flow of the lower lithosphere and implications for slip rates of continental strike-slip faults. *Nature* **391**, 655-659 (1998).

8. P. Molnar, P. Tapponnier, Cenozoic tectonics of Asia: Effects of a continental collision, *Science* **189**, 419-426 (1975).

9. P. England, J. Jackson, Uncharted seismic risk. *Nat. Geosci.* **4**, 348-349 (2011).

10. J. Fang *et al.*, The Dynamics of the India-Eurasia Collision: Faulted Viscous Continuum Models Constrained by High-Resolution Sentinel-1 InSAR and GNSS Velocities, *J. Geophys. Res. Solid Earth* **129**, e2023JB028571 (2024).

11. A. Vauchez, A. Tommasi, D. Mainprice, Faults (shear zones) in the Earth's mantle, *Tectonophysics* **558-559**, 1–27 (2012).

12. M. Kahraman, *et al.*, Crustal-scale shear zones and heterogeneous structure beneath the North Anatolian Fault Zone, Turkey, revealed by a high-density seismometer array, *Earth, Planet. Sci. Lett.* **430**, 129–139 (2015).

13. P. England, D. McKenzie, A thin viscous sheet model for continental deformation. *Geophys. J. Int.* **70**, 295-321 (1982).

14. L. M. Flesch, A. J. Haines, W. E. Holt, Dynamics of the India-Eurasia collision zone. *J. Geophys. Res. Solid Earth* **106**, 16435-16460 (2001).

15. P. C. England, G. A. Houseman, The Mechanics of the Tibetan Plateau. *Philos. Trans. Roy. Soc. A* **326**, 301-320 (1988).

16. P. Tapponnier *et al.*, Oblique stepwise rise and growth of the Tibet plateau. *Science* **294**, 1671-1677 (2001).

17. C. Kreemer, G. Blewitt, E. C. Klein, A geodetic plate motion and global strain rate model. *Geochem. Geophys. Geosyst.* **15**, 3849-3889 (2014).

18. W. Wang, X. Qiao, K. Ding, Present-day kinematics in southeastern Tibet inferred from GPS measurements. *J. Geophys. Res. Solid Earth* **126**, e2020JB021305 (2021).

19. M. Wang, Z.-K. Shen, Present-Day Crustal Deformation of Continental China Derived From GPS and Its Tectonic Implications. *J. Geophys. Res. Solid Earth* **125**, e2019JB018774 (2020).

20. E. Attema *et al.*, Sentinel-1 ESA's new European radar observatory. *EUSAR 2008*, (2008).

21. M. Lazecký *et al.*, LiCSAR: An automatic InSAR tool for measuring and monitoring tectonic and volcanic activity. *Remote Sens.* **12**, 2430 (2020).

22. Y. Morishita *et al.*, LiCSBAS: An Open-Source InSAR Time Series Analysis Package Integrated with the LiCSAR Automated Sentinel-1 InSAR Processor. *Remote Sens.* **12**, 424 (2020).

23. W.-P. Ge, P. Molnar, Z.-K. Shen, and Q. Li, Present-day crustal thinning in the southern and northern Tibetan Plateau revealed by GPS measurements, *Geophys. Res. Lett*. **42**, 5227–5235 (2015) doi:10.1002/2015GL064347.

24. P. Molnar, P. England, J. Martinod, Mantle dynamics, the uplift of the Tibetan Plateau and the Indian Monsoon, *Rev. Geophys.* **31**, 357-396 (1993).

25. M. Lazecky *et al.*, LiCSAR Extra & LiCSBAS. Zenodo. https://doi.org/10.5281/zenodo.17734804 (2025).

26. H. Wang, T.J. Wright, Satellite geodetic imaging reveals high strain away from major faults of Western Tibet. *Geophys. Res. Lett.* **39**, L07303 (2012).

27. Wang, H., Wright, T. J., velmap (v1.1). Zenodo. https://doi.org/10.5281/zenodo.17713962 (2025).

28. J. R. Weiss *et al.*, High-Resolution Surface Velocities and Strain for Anatolia From Sentinel-1 InSAR and GNSS Data. *Geophys. Res. Lett.* **47**, e2020GL087376 (2020).

29. G. Zheng *et al.*, Crustal deformation in the India-Eurasia collision zone from 25 years of GPS measurements. *J. Geophys. Res. Solid Earth* **122**, 9290-9312 (2017).

30. Q. Ou *et al.*, Large-Scale Interseismic Strain Mapping of the NE Tibetan Plateau From Sentinel-1 Interferometry. *J. Geophys. Res. Solid Earth* **127**, e2022JB024176 (2022).

31. H. Ansari, F. De Zan, A. Parizzi, Study of systematic bias in measuring surface

deformation with SAR interferometry. *IEEE Trans. Geosci. Remote Sens.* **59**, 1285-1301 (2020).

32. R. Grandin *et al.*, Long-term growth of the Himalaya inferred from interseismic InSAR measurement. *Geology*, **40**(12), 1059-1062 (2012).

33. Q. Zhao *et al.*, The vertical velocity field of the Tibetan Plateau and its surrounding areas derived from GPS and surface mass loading models. *Earth and Planetary Science Letters*, **609**, p.118107 (2023).

34. S. Liu, S. Jónsson., Glacial isostatic uplift in the Tibetan Plateau and surroundings. *Geophysical Research Letters* **52** (13), e2025GL114899 (2025).

35. G.A. Houseman, P.C. England, L.A. Evans, L.A., Gravitational instability of thickened yet compositionally buoyant Tibetan mantle lithosphere. *Tectonophysics*, **911**, p.230837 (2025).

36. Y. Chen, M. Liu, Correlation between Strain Rate and Seismicity in Different Tectonic Settings, *Seismol. Res. Lett.* **95**, 2375–2385 (2024). doi: 10.1785/0220230306

37. W.-J. Zheng *et al.*, Late Quaternary slip rate of the South Heli Shan Fault (northern Hexi Corridor, NW China) and its implications for northeastward growth of the Tibetan Plateau. *Tectonics* **32**, 271-293 (2013).

38. J. Guo *et al*., Surface ruptures associated with the 1937 M 7.5 Tuosuo Lake and the 1963 M 7.0 Alake Lake earthquakes and the paleoseismicity along the Tuosuo Lake segment of the Kunlun Fault, Northern Tibet. *Bull. Seismol. Soc. Am.* **97**(2), 474-496 (2007).

39. T.J. Wright, 2016. The earthquake deformation cycle. *Astronomy and Geophysics* **54**(7), 4-20.

40. E. Hussain *et al.*, Constant strain accumulation rate between major earthquakes on the North Anatolian Fault. *Nat. Commun.* **9**, 1392 (2018).

41. T. Yamasaki, T. J. Wright, G. A. Houseman, Weak ductile shear zone beneath a major strike-slip fault: Inferences from earthquake cycle model constrained by geodetic observations of the western North Anatolian Fault Zone. *J. Geophys. Res. Solid Earth* **119**, 3678-3699 (2014).

42. B. Meade, Y. Klinger, E.A. Hetland, Inference of multiple earthquake-cycle relaxation timescales from irregular geodetic sampling of interseismic deformation. *Bull. Seismol. Soc. Am.* **103**, 2824-2835 (2013). doi:10.1785/0120130006

43. G.A. Houseman, basil (v1.7.6a). Zenodo. https://doi.org/10.5281/zenodo.10052242 (2023).

44. G. Hirth, D. Kohlstedt, Rheology of the upper mantle and the mantle wedge: A view from the experimentalists. In: Eiler, J. (Ed.), Inside the Subduction Factory, American Geophysical Union (2013).

45. L.J. Sonder, P.C. England, Vertical averages of rheology of the continental lithosphere; relation to thin sheet parameters, *Earth Planet. Sci. Lett.* **77**, 81–90 (1986).

46. C. DeMets, S. Merkouriev, S. Jade, High-resolution reconstructions and GPS estimates of India–Eurasia and India–Somalia plate motions: 20 Ma to the present. *Geophys. J. Int.* **220**, 1149-1171 (2020).

47. C. DeMets, R.G. Gordon, D.F. Argus, Geologically current plate motions. *Geophys. J. Int.* **181**(1), 1–80 (2010).

48. C. Amante, B.W. Eakins, ETOPO1 arc-minute global relief model: procedures, data sources and analysis. (2009).

49. S.M. Chung *et al.*, Tibetan tectonic evolution inferred from spatial and temporal variations in post-collisional magmatism, *Earth-Science Reviews,* 68, 173 – 196 doi:10.1016/j.earscirev.2004.05.001 (2005).

50. L. Ding, P. Kapp, D. Zhong and W. Deng. Cenozoic Volcanism in Tibet: Evidence for Transition from Oceanic to Continental Subduction, *J. Petrology*, 44, 1833-1865 (2003). 10.1093/petrology/egg061

51. S.L. Klemperer. Crustal flow in Tibet: geophysical evidence for the physical state of Tibetan lithosphere, and inferred patterns of active flow, *in*: Law, R.D., M.P. Searle and L. Godin,(eds.) Channel Flow, Ductile Extrusion and Exhumation in Continental Collision Zones. *Geological Society, London, Special Publications*, 268, 39–70 (2006).

52. M. Antolik, R.E.Abercrombie, G. Ekstrom, The 14 November 2001 Kokoxili (Kunlun Shan), Tibet, Earthquake: Rupture transfer through a large extensional step-over, *Bull. Seismol. Soc. Am.* **94**, 1173–1194 (2004). https://doi.org/10.1785/012003180

53. B.P.Allmann, P.M. Shearer, Global variations of stress drop for moderate to large earthquakes, *J. Geophys. Res.* **114** (B1) (2009). doi:10.1029/2008JB005821

54. C.S.Takeuchi, Y. Fialko, Dynamic models of interseismic deformation and stress transfer from plate motion to continental transform faults. *J. Geophys. Res.* **117**, B05403, (2012). doi:10.1029/2011JB009056

55. K. Willis*, et al.*, Strain localization by shear heating and the development of lithospheric shear zones, *Tectonophysics* **764**, 62–76 (2019).

56. J.H.P. De Bresser, J.H. Ter Heege, C.J. Spiers, Grain size reduction by dynamic recrystallization: can it result in major rheological weakening? *Int. J. Earth Sci.* **90**, 28-45 (2001). doi:10.1007/s005310000149

57. L.G.J. Montési, Fabric development as the key for forming ductile shear zones and enabling plate tectonics, *J. Struct. Geol.* (2013). doi:10.1016/j.jsg.2012.12.011

58. J.A. Jackson, H. Austrheim, D. McKenzie, K. Priestley, Metastability, mechanical strength, and the support of mountain belts, *Geology* **32**, 625–628 (2004)

doi:10.1130/G20397.1

59. M. Carpenter, S. Piazolo, T. Craig, T. Wright, Mid-crustal strain localisation triggered by localised fluid influx and activation of dissolution-precipitation creep, *J. Struct. Geol.***199**, 105461, doi: 10.1016/j.jsg.2025.105461 (2025)

60. K.E. Dayem, G.A. Houseman, P. Molnar, Localization of shear along a lithospheric strength discontinuity: Application of a continuous deformation model to the boundary between Tibet and the Tarim Basin, *Tectonics* **28**, TC3002, (2009) doi:10.1029/2008TC002264

61. A.R. Duvall *et al.*, Low-temperature thermochronometry along the Kunlun and Haiyuan Faults, NE Tibetan Plateau: Evidence for kinematic change during late-stage orogenesis, *Tectonics* **32**, 1190–1211 (2013).

62. L.M. Staisch, N.A. Niemi, M.K. Clark, H. Chang, The Cenozoic evolution of crustal shortening and left-lateral shear in the central East Kunlun Shan: Implications for the uplift history of the Tibetan Plateau. *Tectonics* **39**, e2020TC006065 (2020).

63. J. Lee *et al.*, Middle to late Miocene extremely rapid exhumation and thermal re-equilibration in the Kung Co rift, southern Tibet, *Tectonics* **30**, TC2007 (2011).

64. R.H. Styron *et al.*, Miocene initiation and acceleration of extension in the South Lunggar rift, western Tibet: Evolution of an active detachment system from structural mapping and (U-Th)/He thermochronology, *Tectonics* **32**, 880–907 (2013).

65. T.J. Wright *et al*., Deformation, Strains, and Velocities for the Tibetan Plateau from Sentinel-1 InSAR, GNSS, and Levelling Data, version 1. *NERC EDS Centre for Environmental Data Analysis*, https://catalogue.ceda.ac.uk/uuid/6181ff81c7dc4ab2a492c8f53f58df52/, doi:10.5285/6181ff81c7dc4ab2a492c8f53f58df52 (2025).

66. R. Styron, M. Pagani, The GEM global active faults database. *Earthq. Spectra* **36**, 160-180 (2020).

67. T.J. Wright, B. Parsons, Z. Lu, Toward mapping surface deformation in three dimensions using InSAR. *Geophys. Res. Lett.* **31** (2004)

68. P. England, G.A. Houseman, L.Sonder, Length scales for continental deformation in convergent, divergent, and strike-slip environments: Analytic and approximate solutions for a thin viscous sheet model, *J. Geophys. Res. Solid Earth* **90**, 3551-3557 (1985).

69. Yu, C., Li, Z., Penna, N. T., Crippa, P., Generic atmospheric correction model for interferometric synthetic aperture radar observations, *J. Geophys. Res. Solid Earth* **123**(10), 9202-9222 (2018).

70. Z. Yunjun, Fattahi, H., Pi, X., Rosen, P., Simons, M., Agram, P., Aoki, Y., Range geolocation accuracy of C-/L-band SAR and its implications for operational stack coregistration. *IEEE Trans. Geosci. Remote Sens.* **60**, 1-19 (2022).

71. X. Xu, Sandwell, D. T., Toward absolute phase change recovery with InSAR: Correcting for earth tides and phase unwrapping ambiguities. *IEEE Trans. Geosci. Remote Sens.* **58**(1), 726-733 (2019).

72. P. Wessel, Luis, J. F., Uieda, L. A., Scharroo, R., Wobbe, F., Smith, W. H., Tian, D., The generic mapping tools version 6. *Geochem. Geophys. Geosyst.* **20**(11), 5556-5564 (2019).

73. M. Lazecky, Fang, J., Hooper, A., Wright, T., Improved phase unwrapping algorithm based on standard methods. In *IGARSS 2022-2022 IEEE International Geoscience and Remote Sensing Symposium* (pp. 743-746). IEEE (2022).

74. O. L. Stephenson, *et al.*, The impact of plate motions on long-wavelength InSAR-derived velocity fields. *Geophys. Res. Lett.* **49**(21), e2022GL099835 (2022).

75. J. Elliott *et al*., Deformation, Strains and Velocities for the Alpine Himalayan Belt from trans-continental Sentinel-1 InSAR & GNSS. EarthArXiv eprints (2025): https://doi.org/10.31223/X5GX6B.

76. Z. Altamimi, *et al.*, ITRF2014 plate motion model. *Geophys. J. Int.* **209**, 1906–1912 (2017).

77. A. Love, A treatise on the mathematical theory of elasticity. Courier Corporation, (1944).

78. J. Fang *et al*., Strain partitioning in the Southeastern Tibetan Plateau from kinematic modeling of high-resolution Sentinel-1 InSAR and GNSS. Geophysical Research Letters, **51**(19), 2024GL111199 (2024).

Acknowledgments:

COMET is the UK Natural Environment Research Council's Centre for the Observation and Modelling of Earthquakes, Volcanoes and Tectonics, a partnership between UK Universities and the British Geological Survey. We thank the reviewers of an earlier version of this manuscript for their comments which helped us improve this submission.

Funding:

We acknowledge the following funders of this research:

NERC LiCS grant Refs NE/K011006/1, NE/K010867/1 (BP, TJW, GAH, AJH)

COMET National Capability grants 2014/2019/2021 (TJW, GAH, AJH, JRE, BEP)

NERC Earthquakes without Frontiers grant Refs NE/J02001X/1, NE/J01978X/1 (BP, TJW)

Royal Society Fellowship grant Ref URF\R\21106 (JRE)

Royal Society grant RF\ERE\210143 (JRE)

National Natural Science Foundation of China Ref 42274001 (HW).

Author contributions:

Conceptualization: TJW, GAH, JF, BP

Methodology: TJW, GAH, JF, YM, AJH, LE, ML, QO, CR, HW, DW

Investigation: TJW, GAH, JF, YM, DW

Visualization: TJW, GAH, JF

Funding acquisition: TJW, BP, JRE

Writing – original draft: TJW, GAH

Writing – review & editing: All

Competing interests: Authors declare that they have no competing interests.

Data and materials availability: GNSS and levelling data, LOS velocities, LiCSBAS processing parameters, 3D velocity grids, strain rates and *velmap* outputs created and used in this study are available in CEDA repository: doi:10.5285/6181ff81c7dc4ab2a492c8f53f58df52 (*65*). All other data needed to evaluate the conclusions in the paper are present in the paper or the supplementary materials. No new physical materials were generated for this study.

SUPPLEMENTARY MATERIALS

Materials and Methods

Figs. S1 to S19

References (*67*-*78*)

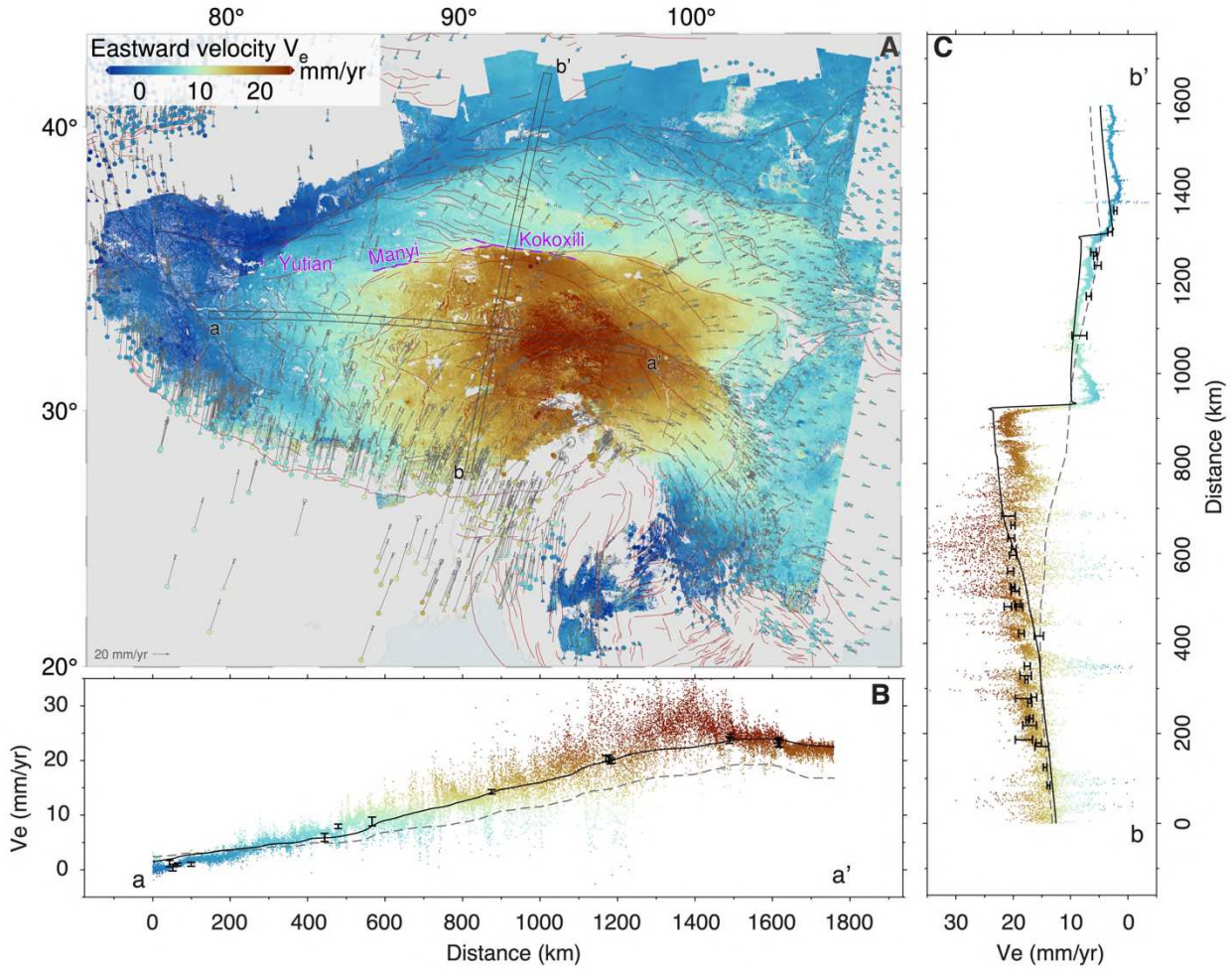

Fig. 1. High-resolution velocity field of Tibet. (A) East component of the velocity field for Tibet derived from the geo-referenced InSAR, overlain with velocity vectors from GNSS observation points marked by colored circles (2D sites) and triangles (3D) (*SM.4*), relative to a fixed Eurasia reference frame. Faults, shown as dark red lines, are from the Global Earthquake Model (*66*), with purple dashed lines indicating the ruptures of the 1997 Manyi and 2001 Kokoxili earthquakes, associated with the Kunlun fault zone, and 2008 and 2014 Yutian earthquakes, associated with the Altyn Tagh fault zone (Fig. 2C). (B), (C) profiles of the eastward velocity component along lines marked a-a' and b-b' in (A). Colored dots are east velocities from the InSAR grid within 15 km of the profile line; black bars show GNSS east velocities within 100 km of the profile and their formal uncertainties (±1 standard deviation; *SM.4*); the solid black line is the prediction of our best-fit geodynamic model (*SM.7*); the gray dashed line is the best geodynamic model we obtained without including faults.

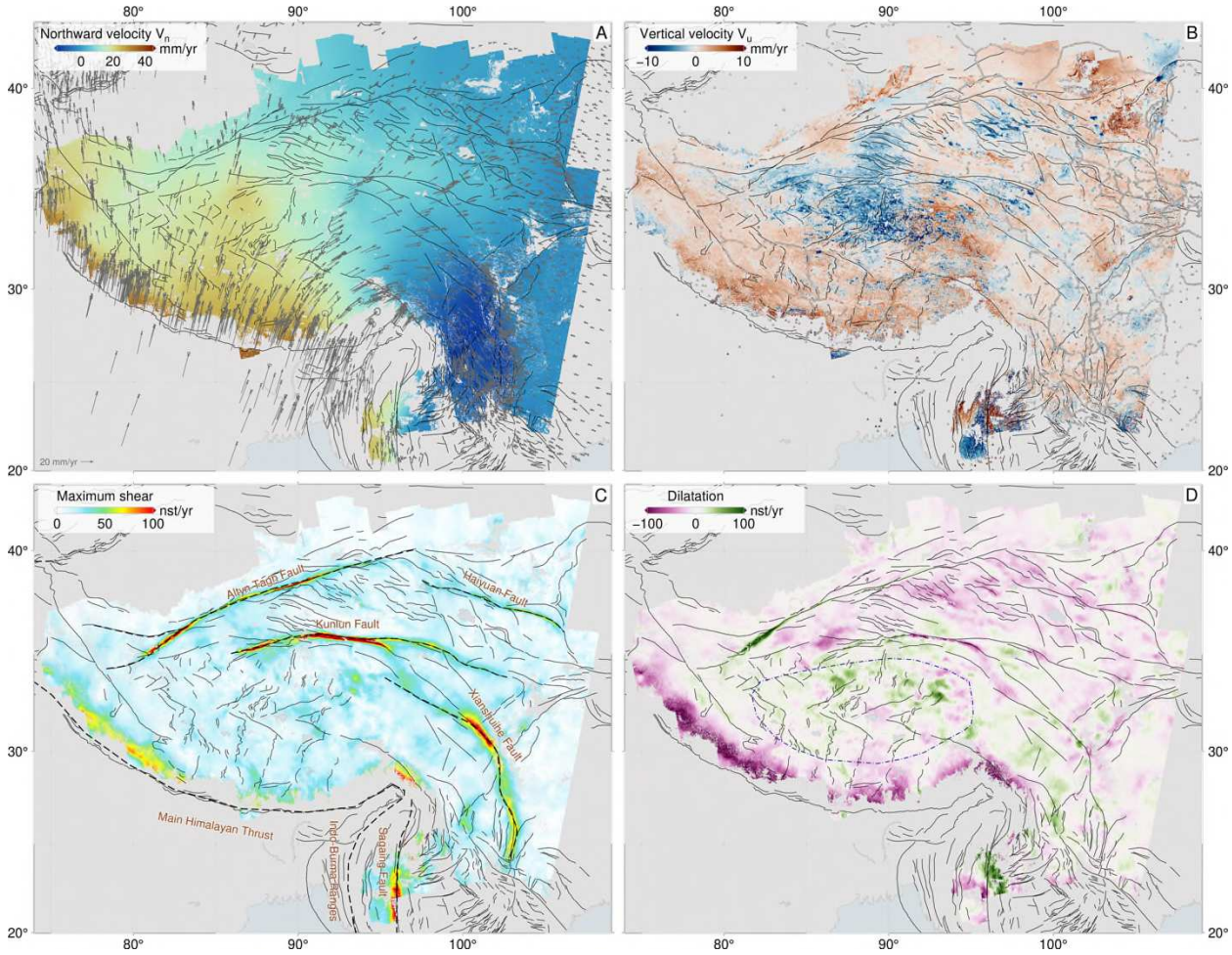

Fig. 2. Components of the estimated horizontal strain rate field. (A) Northward velocity field from the *coarse* velocity model, overlain with GNSS horizontal velocity vectors. (B) High-resolution vertical velocity field derived from geo-referenced InSAR, constrained by vertical GNSS measurements (colored triangles) and levelling data (circles) (Fig. S2). (C) Maximum shear strain rate (nanostrain/yr) and (D) horizontal dilatation rate (green=expanding; purple=contracting) derived from gradients of the InSAR data (*SM.5*). Thick dashed black lines in (C) show the major faults we include in our geodynamic model; thin black lines are from the Global Earthquake Model (*66*). The dotted blue region in (D) defines the area used for calculating average strain rate cited in the text.

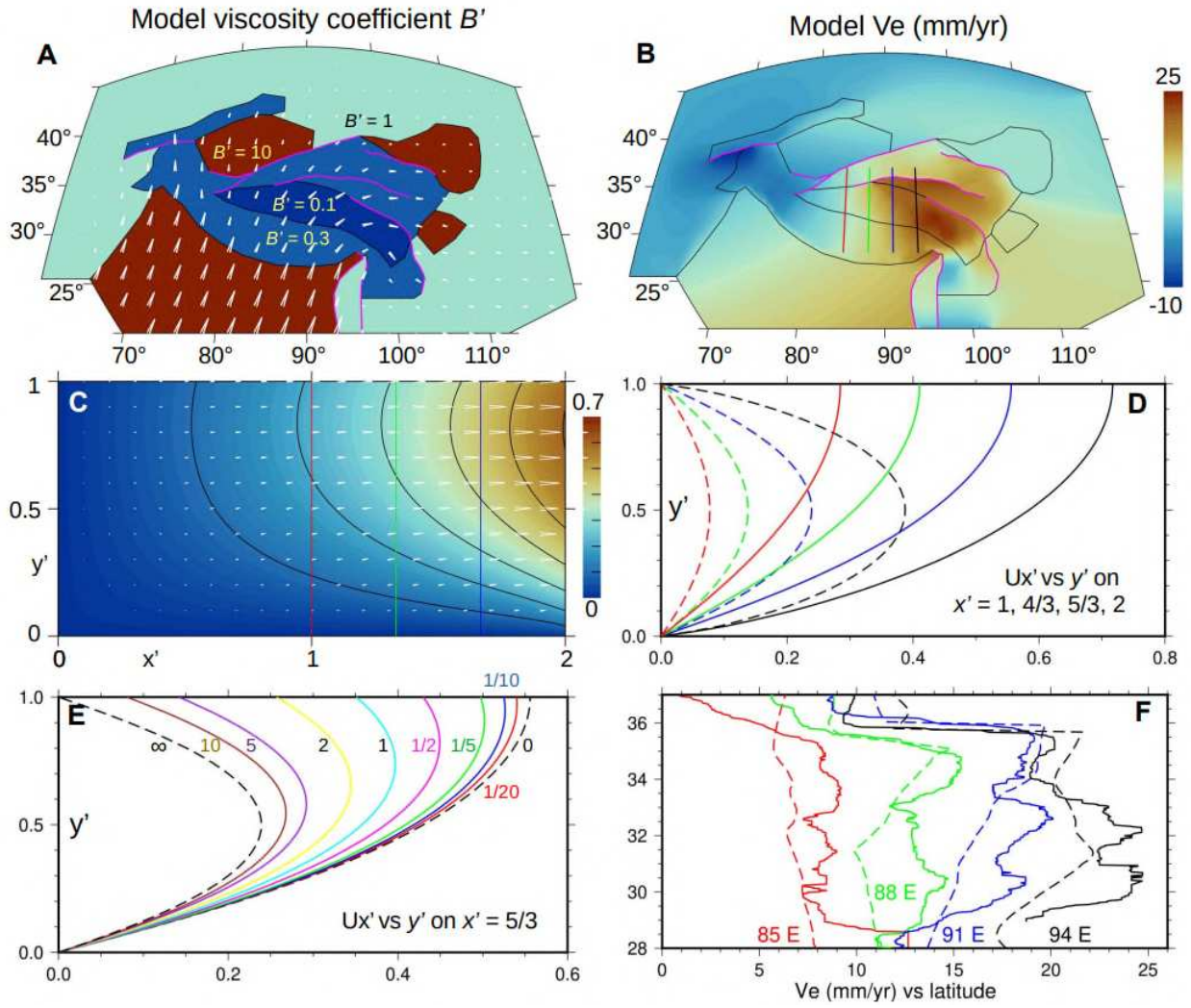

Fig. 3. Comparison of observed and modelled eastward velocity fields. (A) Regional variation of viscosity coefficient used in the preferred thin viscous shell model (*10*); black lines represent regional boundaries and magenta lines are model faults; the model velocity field is indicated by white arrows; (B) East component of the model velocity field V_e (mm/yr), for comparison with observed V_e (Fig. 1), (C) Simplified conceptual model showing velocity in the x' direction, $U_{x'}$, within a uniform rectangular region $0 \le x' \le 2; 0 \le y' \le 1$ with outflow on $x' = 2$ driven by a step in gravitational potential energy, and boundary $y' = 1$ representing a fault with resistance coefficient $f' = 0.5$, (D) y-direction profiles of $U_{x'}$ on $x' = 1, 4/3, 5/3, 2$ of the simplified model for $f' = 0$ (solid lines) and f' = infinity (dashed lines), (E) y-direction profiles to show effect on $U_{x'}$ at $x' = 5/3$, of the boundary f' varied between 0 and ∞. (F) scaled profiles of observed V_e (solid lines) compared to V_e computed from thin viscous shell model (dashed lines) at constant longitude profiles marked on (B).

Science
AAAS

Supplementary Materials for

High-resolution geodetic velocities reveal role of weak faults in deformation of Tibetan Plateau

Authors: T.J. Wright[1]*, G.A. Houseman[2,1], J. Fang[1]*, Y. Maghsoudi[3], A.J. Hooper[1], J.R. Elliott[1], L. Evans[4], M. Lazecky[1], Q. Ou[5], B.E. Parsons[6], J.C. Rollins[7], L. Shen[8], H. Wang[9], D. Wang[1]

Affiliations:

[1] COMET, School of Earth and Environment, University of Leeds, Leeds, UK
[2] State Key Laboratory of Deep Earth Exploration and Imaging, China University of Geosciences, Beijing, China
[3]COMET, Department of Earth and Environmental Sciences, University of Exeter, Penryn, UK
[4] School of Earth, Atmosphere & Environment, Monash University, Clayton, VIC, Australia
[5] COMET, School of GeoSciences, University of Edinburgh, Drummond, Edinburgh, UK
[6] COMET, Department of Earth Sciences, University of Oxford; Oxford, UK
[7] GNS Science, Lower Hutt, New Zealand
[8] Lamont-Doherty Earth Observatory, Columbia University, New York, USA
[9] College of Natural Resources and Environment, South China Agricultural University, Guangzhou, China

*Corresponding author. Email: t.j.wright@leeds.ac.uk (T.J.W.); j.fang@leeds.ac.uk (J.F.)

This PDF file includes:

Materials and Methods

1. InSAR processing

We processed data from ~44,500 Sentinel-1 SAR acquisitions to create ~341,400 interferograms using the COMET-LiCSAR system (*21*). This system was built to automatically create Sentinel-1 interferograms from 250-km-wide Interferometric Wide Swath data acquired over the continents. We divide that land surface up into 127 ascending and 114 descending frames that are typically 250 km long, and process interferometric networks in short-baseline configurations, typically aiming to connect each epoch to the closest 4 epochs in time, adding in 6-month and 12-month interferograms to minimize the impact of phase bias. In Tibet, most data were acquired with a 12-day revisit. We define some frames to be larger than the 250 km standard definition, typically where frame boundaries coincide with major faults, or where boundaries needed to be adjusted to coincide with a switch from Sentinel-1A to -1B. All interferograms are available in Geotiff format via the COMET-LiCSAR portal (https://comet.nerc.ac.uk/comet-lics-portal/) and via the CEDA archive (https://data.ceda.ac.uk/neodc/comet/data/licsar_products). Individual networks used for time series analysis in each frame are also available via the CEDA archive (*66*).

2. Estimating average line-of-sight velocities

We correct the LiCSAR data for modeled troposphere (*69*), ionosphere (*70*) and earth tides (*71, 72*), and down-sample during an updated unwrapping procedure (*73*) from ~100 m to ~1 km resolution. We calculate average line-of-sight velocities for each LiCSAR frame using the LiCSBAS code *(22,25)*, which finds the best fit long-term velocity on a pixel-by-pixel basis, using the available short-baseline network. The approach accounts for any gaps in the network and identifies and removes unwrapping errors found by checking closure phase around triangular loops. We additionally performed a careful visual inspection to remove all the remaining poor-quality interferograms prior to the LiCSBAS inversion. After the inversion, we masked noisy pixels using noise indices, including the number of unclosed loops and the RMS of residuals in the small baseline inversion; we adjusted these parameters for each frame to optimize the results. We further flattened the bootstrapping-derived velocity standard deviation, using semi-variogram analysis to remove the impact of distance from the reference area (*30*). Additionally, we estimated and subtracted the motion of the Eurasian plate from all frames (*74*). Some of the key processing parameters are listed at (*66*).

The line-of-sight velocities for all the frames used in this analysis are available to download from the CEDA archive (*66*).

3. Correcting for earthquakes

To correct for earthquakes that occurred in the time period of the observations, we solve for a step in the line-of-sight displacements and use the average line-of-sight velocities excluding the coseismic displacements. We apply this correction to earthquakes larger than M6. The exception is M_w 7.3 Maduo Earthquake in Southern Qinghai, China, which was the only earthquake larger than M_w 7 that occurred in our observation period. For the frames impacted by this earthquake, we truncate the time series and only present the inter-seismic velocities measured before the earthquake. Details of any earthquake corrections applied to individual frames are provided on the CEDA archive (*66*).

4. GNSS and levelling compilation

We compile 18,203 GNSS velocities and 6,607 levelling rates (plus 4 SLR, 2 DORIS and 2 VLBI velocities) in the vicinity of the Tibetan Plateau (73.5 to 112ºE and 20 to 45ºN) from 131 studies and datasets published since 2013 (data and studies listed at *66*). We prepare and combine these velocities in a multi-step procedure summarized below. More details are provided in *(75)*.

1. First, we transform each input dataset into the ITRF2014 Eurasia-fixed reference frame *(76)*.

2. Next, we improve the precision of some GNSS velocities whose locations are rounded to the nearest 0.1° or 0.01°, by linking velocities in different datasets that are at the same site and using the highest-precision location available for each linked site.

3. We identify 14 velocities that do not have uncertainties provided but do have site occupation durations and numbers of occupations evident, and we use these metadata to estimate the velocity uncertainties with a model that combines random-walk, white and flicker noise. We also round up unrealistically small positive uncertainties to a minimum of 0.05 mm/yr for the east and north components (the 2.275th-percentile or -2σ value of all compiled east and north uncertainties) and 0.12 mm/yr for the vertical component (the -2σ value of compiled vertical uncertainties). This rounding is applied to 129 east, 108 north and 107 vertical uncertainties.

4. We then begin flagging and removing outlier velocities. We first flag 71 velocities that have site occupation times of <1.5 yr, east or north uncertainties of >5 mm/yr (the $+3\sigma$ value of the compiled east and north uncertainties), vertical uncertainties of >24 mm/yr (the $+3\sigma$ value of compiled vertical uncertainties), or uncertainties that are zero or remain undefined.

5. We then use an iterative automated approach to flag other outlier velocities. For each velocity in the dataset, we find the population of velocities at nearby sites and compute a central value (halfway between the median and mean) and mean absolute deviation (MAD) of that population's velocities in both the east and north components. We flag outliers as velocities that deviate from the central value by more than a scalar multiple of the MAD (in either the east or north component). The multiple of the MAD is started at a relatively high value to detect the most obvious outliers first (and exclude them from the nearby population in subsequent iterations), then iteratively brought down to a final preferred value of 3.75. This flags 432 outliers in total, which are then removed.

6. Next, we use another iterative method to remove remaining systematic velocity differences between datasets (arising from their uses of different stations to get into their original reference frames). For each study or dataset, we tabulate the differences between that study's velocities and all other studies' velocities at any common sites, fit those differences to an Euler-pole rotation using least squares, and apply 1/20 (5%) of that rotation to that study, then move on to the next study. After proceeding through all of the studies, we recalculate all of the velocity differences and run another iteration. This is done for 200 total iterations (100 in which compilation studies such as *(19)* are treated as single studies, and a second 100 in which they are split out into their constituent studies, by which time the rotations being applied are extremely small).

7. After alignment, we reapply the automatic outlier detector to identify and remove 90 other outliers that become apparent in the aligned field. We also remove 1,886 velocities that are based entirely on data preceding the Sentinel-1 era (2014-present) and are superseded by newer, high-quality measurements at the same locations, plus 1,349 other duplicate velocities. This leaves 14,373 GNSS velocities.

8. Finally, we combine collocated GNSS velocities by (for each component) computing a central value that lies halfway between the mean and the median of the velocities being combined. We compute several alternate measures of uncertainty on this central value, exploring three "meta-uncertainties": whether to take into account the uncertainties on the velocities being combined, whether to treat different studies' velocities at the same site as independent data or not, and whether to use the standard deviation or the mean absolute deviation as the measure of spread. These three different either-or options imply eight different metrics of uncertainty on the mean velocity and a separate eight for the median, or 64 different possible uncertainty metrics on the average of the mean and median. We compute the combined uncertainty that would result from each of these 64 different metrics, then take the average of the mean and median of those 64 as the final uncertainty (for each component, at each station with multiple velocities).

For purposes of our modelling, we also discard vertical velocities with absolute values exceeding 20 mm/yr from the final combined dataset; however, these may be useful for other studies of nontectonic processes. The final combined point-velocity dataset (available at *66*) includes 3142 horizontal velocities (from 1707 2D and 1435 3D GNSS sites) and 7767 vertical rates (from 1435 3D and 70 pure vertical GNSS, as well as 6262 levelling rates) in the study region (Fig. S2).

The GNSS data format columns are as follows:

2D dataset: longitude; latitude; eastward and northward velocities; 1-sigma uncertainties in the eastward and northward components; east-north covariance (assumed zero); station type (GNSS); station name; study identifier.

3D dataset: longitude; latitude; eastward, northward, and vertical velocities; 1-sigma uncertainties in the eastward, northward, and vertical components; the three velocity covariances (all assumed zero); station type (GNSS or levelling); station name; study identifier.

For purely vertical GNSS and levelling data, horizontal velocities are assumed zero with a large uncertainty of 1,000,000 mm/yr.

GNSS stations and the plotted profiles in Fig. 1B,1C can be extracted from the GNSS data file with the following command using the generic mapping tools software (*72*):

```
gmt project $gnssfile -C79.25/33.51 -E98.02/32.14 -Q -Lw -Fxypz -W-50/50 > gnss_prof_a.txt

gmt project $gnssfile -C90.38/27.67 -E93.82/41.75 -Q -Lw -Fxypz -W-50/50 > gnss_prof_b.txt
```

5. Velocity field generation

To create a unified, coarse velocity field that fits the GNSS, levelling and InSAR data, and which we will refer to as the *coarse* velocity model, we follow the procedure developed by *(26)*. We first establish a triangular mesh covering the region of interest, using a set of nodes spaced by ~0.20 degrees in longitude and latitude (Fig. S1). We then use the *velmap* code *(27)* to invert simultaneously for the best-fit 3D velocities at each node (Fig. S3), reference frame adjustment parameters for each InSAR frame, and a linear-with-height atmospheric correction term for each frame. The reference frame adjustment parameters consist of a second-order polynomial surface. Before inverting for the velocity field, InSAR data are downsampled to 5 km resolution.

As described in *(26)*, velocities at observation points (in the InSAR and GNSS) are linked to the velocities at the nodes of the mesh using linear interpolation functions, which account for variations in the satellite line of sight, and we minimize the weighted square misfit between the observations and predictions. Regularization is applied using Laplacian smoothing to ensure a physically meaningful solution and to handle data gaps.

The derived reference frame adjustment parameters enable us to create mosaics of ascending and descending line-of-sight velocities in a Eurasia reference frame, at the 1 km resolution, and including the linear-with-height atmospheric correction (Fig. S4). We can then invert pixel-by-pixel for the east-west (Fig. 1) and vertical velocities (Fig. S5) directly from the referenced line-of-sight velocities, using the north-south velocities from the *coarse* 3D velocity model (Fig. S3a) as a constraint; InSAR has minimal sensitivity to the north-south velocities, but any error in the north-south velocity field will propagate into an error in the vertical velocities *(67)*.

We calculate strain and rotation rates (Figs. 2, S6,S7) by first taking the horizontal gradients of both the east-west velocities at InSAR resolution (Fig.1) and the north-south velocities derived from the *coarse* velocity model (Fig. S3a). We derive the second invariant ($\dot{\varepsilon}_{II_h}$), maximum shear ($\dot{\varepsilon}_{shear}$), dilatation ($\dot{\varepsilon}_{dil}$), and vorticity ($\dot{\omega}$) components of the horizontal strain rate tensor ($\dot{\varepsilon}_h$), as defined in Equations S1-S5 (which include the spherical correction terms; *77*). To match the spatial resolution in both directions, which minimizes on-fault strain artefacts arising from having different resolutions (e.g. Fig. S14 in *78*), we apply a 150 km median smoothing filter to the east-west velocities with parameters chosen to optimize the tradeoff between spatial resolution and noise (Fig. S8).

$$\dot{\varepsilon}_h = \begin{bmatrix} \dot{\varepsilon}_{xx} & \dot{\varepsilon}_{xy} \\ \dot{\varepsilon}_{yx} & \dot{\varepsilon}_{yy} \end{bmatrix} = \begin{bmatrix} \dfrac{\partial V_E}{\partial x} - \dfrac{V_N}{r}\dfrac{\cos\theta}{\sin\theta} & -\dfrac{1}{2}\left(\dfrac{\partial V_E}{\partial y} + \dfrac{\partial V_N}{\partial x} + \dfrac{V_E}{r}\dfrac{\cos\theta}{\sin\theta}\right) \\ -\dfrac{1}{2}\left(\dfrac{\partial V_N}{\partial x} + \dfrac{\partial V_E}{\partial y} + \dfrac{V_E}{r}\dfrac{\cos\theta}{\sin\theta}\right) & \dfrac{\partial V_N}{\partial y} \end{bmatrix} \quad \text{(S1)}$$

$$\dot{\varepsilon}_{II_h} = \sqrt{\dot{\varepsilon}_{xx}^2 + 2\dot{\varepsilon}_{xy}^2 + \dot{\varepsilon}_{yy}^2} \quad \text{(S2)}$$

$$\dot{\varepsilon}_{shear} = \sqrt{\dot{\varepsilon}_{xy}^2 + \frac{(\dot{\varepsilon}_{xx} - \dot{\varepsilon}_{yy})^2}{4}} \quad \text{(S3)}$$

$$\dot{\varepsilon}_{dil} = \dot{\varepsilon}_{xx} + \dot{\varepsilon}_{yy} \quad \text{(S4)}$$

$$\dot{\omega} = \frac{\partial V_N}{\partial x} - \frac{\partial V_E}{\partial y} \quad \text{(S5)}$$

where V_E and V_N are the eastward and northward velocities, respectively, θ is the colatitude of each pixel, and r is the Earth's radius (r=6378 km).

6. Data weighting and uncertainty estimation

We weight data sets using the uncertainties for the GNSS/levelling velocities (*SM.4*) and the uncertainty in the line-of-sight velocities estimated (pixel-by-pixel) by LiCSBAS *(22,25)*. We downsample InSAR data to 5 km before carrying out the velocity field inversion, and we include spatial covariances in the InSAR data in the inversion.

We exploit the fact that we have redundant and independent InSAR observations in many locations, due to overlapping tracks, to obtain an informal estimate of the uncertainties in the Eurasian-referenced InSAR and in the high-resolution (pixel by pixel) east-west and vertical velocities. For pixels where we have 4 independent observations of line-of-sight velocity (2 ascending tracks and 2 descending tracks), we can calculate 4 estimates of the east-west and vertical velocities, each using data from a single ascending and single descending track (i.e. A1+D1; A1+D2; A2+D1; A2+D2). From these, we can make 2 sets of maps that show the differences between inversions that use independent InSAR data (i.e. A1+D1 vs A2+D2, A1+D2 vs A2+D1). These differences have standard deviations of 2.2 and 2.1 mm/yr in east-west and 1.8 and 1.9 mm/yr in vertical (Fig. S9). If we assume that these differences result from noise that is split equally between the independent estimates, and that the uncertainties have zero mean, we can relate the variance in the difference grid to the uncertainties in each of the independent inversions. This gives uncertainties in east-west and vertical velocities for pixels where only two data sets exist of ~1.5 and ~1.3 mm/yr, respectively. This approach ignores any systematic long-wavelength uncertainty that might arise from the GNSS data, which is common to all inversions.

For pixels where three line-of-sight data sets exist (*i.e.*, 2 ascending + 1 descending; 1 ascending +2 descending), we can exclude one of the redundant data sets and calculate the standard deviation of the difference between the velocity of the excluded data set, Vel_r, and the line-of-sight velocity predicted for that excluded geometry from the eastward and vertical field generated with the remaining two data, Vel_p. These are 2.5 mm/yr when excluding data from an ascending track and 2.3 mm/yr when excluding data from a descending track (Fig. S10). We can calculate the uncertainty on Vel_p as

$$\sigma_{Vel_p} = \sqrt{\left(los_e \sigma_{v_e}\right)^2 + \left(los_n \sigma_{v_n}\right)^2 + \left(los_u \sigma_{v_u}\right)^2} \quad \text{(S6)}$$

where *los* and σ_v are the components of the unit vector and uncertainties for the east, north, and up components. We use the values estimated above of 1.5 and 1.3 mm/yr for σ_{v_e} and σ_{v_u}, respectively, and use a conservative value of 3 mm/yr for σ_{v_n}, as north-south velocities are derived predominately from GNSS. From this information we can then estimate the average uncertainties on the original line-of-sight velocities, which are ~1.4 mm/yr for both the ascending and descending geometry. This compares well to the standard deviation of the residual between the InSAR data and the predicted velocities from the *coarse* velocity model, which has a value of 1.6 mm/yr, and is a more realistic estimate than the formal uncertainties from LiCSBAS, which are typically in the range 0.1 to 0.6 mm/yr (95% confidence).

Finally, we propagate uncertainties in the line-of-sight velocities to uncertainties in east-west and vertical velocities using the standard equations (*67*), to make maps of the uncertainty in the east and vertical velocities. The final spatial distributions of uncertainties are a function of the number of data sets and the viewing geometries at an individual pixel and range from 1.3 to 2.0 mm/yr and 1.0 to 1.5

mm/yr for the eastward and vertical uncertainties, respectively (95% confidence intervals) (Fig. S11). The comparison between InSAR-derived velocities and GNSS/levelling data shows an RMS of 2.2 mm/yr for eastward velocity and 1.8 mm/yr for vertical velocity, with 2.2 mm/yr for vertical GNSS and 1.7 mm/yr for levelling data, respectively (Fig. S12).

Our estimates of strain rates for the Sichuan basin (enclosed by the gray dashed line in Fig. S6d), where tectonic deformation is slow, are of 6 nanostrain/yr in shear strain, 1 nanostrain/yr in dilatation, and 9 nanostrain/yr in the second invariant of the strain rate – these are likely a combination of a small amount of real strain and noise in the data.

7. Simplified conceptual model analysis

We obtained numerical solutions (*10*) for deformation of the thin spherical shell using the finite element method with a model geometry that approximates the actual geographical distribution of the India-Asia collision, including variation of rheological properties and disposition of major active faults based on the geodetic strain rate field. The model that best matches the geodetic velocity field obtained by Fang et al. (*10*), and shown in Fig. 3*a,b* and Fig. S15, generally requires that the major fault systems are weak in terms of the fault resistance coefficient *f*. To demonstrate more clearly why this is, we consider here a simplified model system which includes only the essential elements of a weak fault bounding a flow driven by an excess of gravitational potential energy.

We solve the governing equations for the thin viscous sheet in plane Cartesian coordinates, assuming constant viscosity $n = 1$ and $B = 2\eta_0$ in Eq. (1), and no variation of gravitational potential energy Γ within a rectangular region $0 \le x \le S$, $0 \le y \le W$. This domain represents roughly the region bounded in the south by the Himalayas between about 85ºE and the eastern syntaxis, and in the north by the Kunlun Fault system. Similar to the actual displacement field, we represent a velocity field in which the north (y) component of velocity, is approximately zero ($v = 0$ on all 4 boundaries). We set $S = 2W$ as representative of the region and impose $u = v = 0$ on the west (x=0) boundary. We also assume that the north (y=W) boundary represents a fault on which Eq. (2) applies, with Δu here representing the velocity relative to a rigid external region. We assume in each case that deformation is driven by a constant x-direction "pull" σ_T on the boundary $x = S$, and note also that the external pull can mimic exactly the effect of a step-wise decrease in gravitational potential energy across the east (x=S) boundary, $\Delta\Gamma = L\sigma_T$, where L is the lithospheric thickness. For these calculations with constant viscosity, we have used dimensionless variables: for distance $(x', y') = (x, y)/W$, viscosity $\eta' = \eta/\eta_0$, stress $\sigma'_{ij} = \sigma_{ij}/\sigma_T$ and velocity $u' = u\,\eta/(W\,\sigma_T)$. The dimensionless fault resistance coefficient is then $f' = (W/\eta)f$.

Fig. S18 shows the variation of the east (x) component of velocity within the region for various boundary conditions on north and south boundaries. In Case 1 (Fig. S18*a*) we impose zero shear stress $\tau' = 0$ on both $y' = 0$ and $y' = 1$ boundaries; *u'* then increases linearly from zero at *x'* = 0 to a maximum velocity $u'_{max} = 1$ on $x' = S/W$. Case 1 serves as a reference value against which the other cases may be compared. For Case 2 ($u' = 0$ on both north and south boundaries; Fig. S18*b*) the maximum velocity is only about 0.39 and it decays rapidly with distance from the east boundary. For Case 3 (Fig. S18*c*), with $u' = 0$ on the south boundary and $\tau' = 0$ on the North boundary, the maximum flow velocity reaches about 0.72 on the north-east corner. Relative to Case 2, the stress-free northern boundary mobilises a much more extensive part of the region to participate in the flow, mainly in the region adjacent to that boundary. Cases 1 to 3 are consistent with the fault condition on the

northern boundary if $f' = 0$ (Case 3) or $f' \to \infty$ (Case 2), and we show three more cases (Fig. S18*d,e,f*) with f' = 0.2, 1 and 5 respectively which, as expected, show solutions that are gradational between Cases 2 and 3. The fault-like boundary condition clearly enables a much greater part of the region away from the $x = S$ boundary to be activated for eastward flow as f' is decreased. The approximate analytic solutions described in the next section explain the change in effective length scale of the solution, from S in Case 1 to W in Case 2, to $2W$ in Case 3.

Fig. S19a shows the systematic variation of $u'(y')$ at x' = 1.75, for f' between 0.05 and 10, together with the limiting cases of $f' = 0$ and $f' \to \infty$. We see that in Fig. S19a, $f' \approx 2$ results in the slip velocity on the $y' = 1$ boundary reaching about half of the amplitude obtained for the zero shear-stress case. When scaled to dimensional values, the magnitude of the velocity depends on viscosity and boundary traction also, but the shape of the y (north-south) profile of the x (east) component of velocity is simply diagnostic of the magnitude of f' on the northern boundary. We repeated the calculations using a non-linear rheological law representative of depth-averaged lithospheric deformation with n = 3, and constant coefficient B. Comparison of Fig. S19a (n = 1, constant viscosity) and Fig. S19b (n = 3, power-law viscosity) shows that in both cases the fault-like boundary condition has a similar impact as f is varied between 0 and ∞. For both n = 1 and n = 3, the maximum velocity for Case 2 is about half that for Case 3, but it is clear for Case 2 that the velocity decays more quickly with distance from the $x = S$ boundary for n = 3, as found by (*68*).

8. Related analytical solutions for thin viscous sheet model

In what follows we provide approximate analytical solutions for the constant viscosity case that shed light on the results of the preceding section. The x-component of the thin viscous sheet formulation for the simplified problem may be expressed:

$$2\frac{\partial \tau_{xx}}{\partial x} + \frac{\partial \tau_{yy}}{\partial x} + \frac{\partial \tau_{xy}}{\partial y} = \frac{1}{L}\frac{\partial \Gamma}{\partial x} \tag{S7}$$

where Γ is the gravitational potential energy, L is the thickness of the sheet, and $\tau_{\alpha\beta}$ are the components of the depth-averaged horizontal stress tensor in the (x,y) plane. If we assume a Newtonian viscous constitutive law with viscosity η, and negligible motion in the y-direction we obtain the following differential equation for the eastward component of velocity:

$$4\frac{\partial^2 u}{\partial x^2} + \frac{\partial^2 u}{\partial y^2} = \left(\frac{1}{\eta L}\right)\frac{\partial \Gamma}{\partial x} \tag{S8}$$

If we ignore gradients of gravitational potential energy within the plateau, the equation is reduced to a simple homogeneous partial differential equation, and separation of variables gives the following general solution:

$$u(x,y) = \left[A\cosh\left(\frac{Cx}{2}\right) + B\sinh\left(\frac{Cx}{2}\right)\right]\left[E\cos(Cy) + F\sin(Cy)\right] + Dx + Gy + Hxy \tag{S9}$$

and the shear stress τ_{xy} is:

$$\tau_{xy} = \eta C[\sinh(\frac{Cx}{2})][-E\sin(Cy) + F\cos(Cy)] + \eta Hx \quad \text{(S10)}$$

where C^2 is a separation constant that is constrained by boundary conditions, along with the other integration constants *A, B, D, E, F, G* and *H* that are determined when the boundary conditions are specified. We obtain approximate solutions for the domain $0 \leq x < S$ and $0 \leq y \leq W$, and assume that deformation is driven by an *x*-direction "pull" σ_T on the boundary $x = S$, noting that the external pull can represent the effect of a step-wise decrease in gravitational potential energy across this boundary.

For Case 1 in which zero shear stress is applied to the boundaries $y = 0$ and $y = W$, and $C = 0$

$$u(x) = \frac{\sigma_T S x}{4\eta} \quad \text{(S11)}$$

as illustrated in Fig. S18a.

For Case 2 in which the velocity on both horizontal boundaries is zero: (Fig. S18b) and $C = \pi/W$, so

$$u = \frac{W\sigma_T}{2\pi\eta}[\frac{\sinh(\pi x/(2W))}{\cosh(\pi S/(2W))}][\sin(\frac{\pi y}{W})] \quad \text{(S12)}$$

if the outward pull on $x = S$ is:

$$\sigma_{xx} = \sigma_T \sin(\frac{\pi y}{W}) \quad \text{(S13)}$$

As in the preceding case, the peak amplitude is proportional to the magnitude of the boundary force and inversely proportional to viscosity. However, contrary to Case 1, $u_{\max}$ is approximately proportional to *W* (rather than *S*). The effect of neglecting the *y*-component of velocity in deriving Eq. (S12) means that (S12) underestimates the maximum *u* in the 2D solution by about 7%. For Fig. S18 we used the same constant traction boundary condition on $x = S$ in each Case, in order that our comparison of rate and distribution of the outward flow is due only to changes of the *y* boundary conditions. Higher harmonics ($C = 3\pi/W, 5\pi/W$, etc.) are then present in the solution because of the constant boundary traction we use, but they have only a minor effect on the velocity near the boundary and decay rapidly with distance into the solution domain. Relative to the case where the forcing traction is constant in *y*, (S13) underestimates the maximum displacement rate by about 18%.

In Case 3 the mix of boundary types with zero velocity on $y = 0$ and zero shear stress on $y = W$ (Fig. S18c) requires that $C = \pi/(2W)$, so both the *y*-direction wavelength and the decay of velocity in the *x*-direction are doubled relative to Case 2, and the solution has the form:

$$u = \frac{W\sigma_T}{\pi\eta}[\frac{\sinh(\pi x/(4W))}{\cosh(\pi S/(4W))}][\sin(\frac{\pi y}{2W})] \quad \text{(S14)}$$

for the boundary traction

$$\sigma_{xx} = \sigma_T \sin(\frac{\pi y}{2W}) \quad \text{(S15)}$$

For those cases in which we assume that shear stress is proportional to *u* on the north boundary, with fault resistance coefficient *f*, we take the ratio of shear stress and velocity on $y = W$ to obtain:

$$\frac{\tan(CW)}{C} = \frac{\eta}{f} \tag{S16}$$

and the smallest value of C for which that equation holds ($\pi/(2W) \leq C \leq \pi/W$) provides the fundamental harmonic for arbitrary f. Allowing for the different wave-number C, the solution for arbitrary f appears similar to the solution for Case 3 (Eq. S14) but, as Fig. S19 and Fig. 3d indicate, the maximum eastward velocity on $x = S$ decreases smoothly and the location of that maximum moves from $(x, y) = (S, W)$ to $(x, y) = (S, W/2)$, as f varies from 0 to ∞.

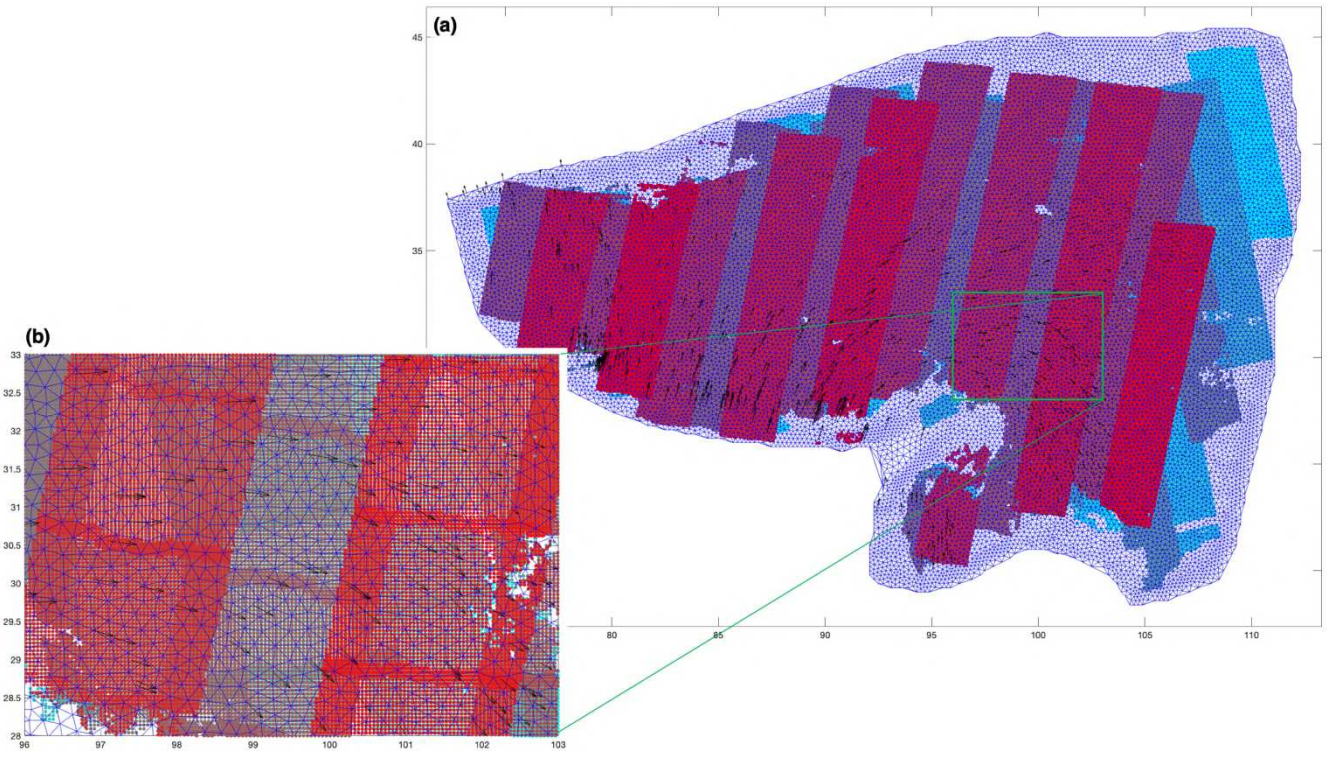

Fig. S1

(a) Mesh and data used for the *coarse* velocity model inversion. The blue lines show the element of the triangular mesh, with black arrows showing the GNSS data used (see Fig. S2). Colored dots show the location of coherent InSAR data used in the inversion. Different tracks are shown in different colors; colors have no other meaning. (b) Close-up of the mesh corresponding to the green rectangle shown in (a).

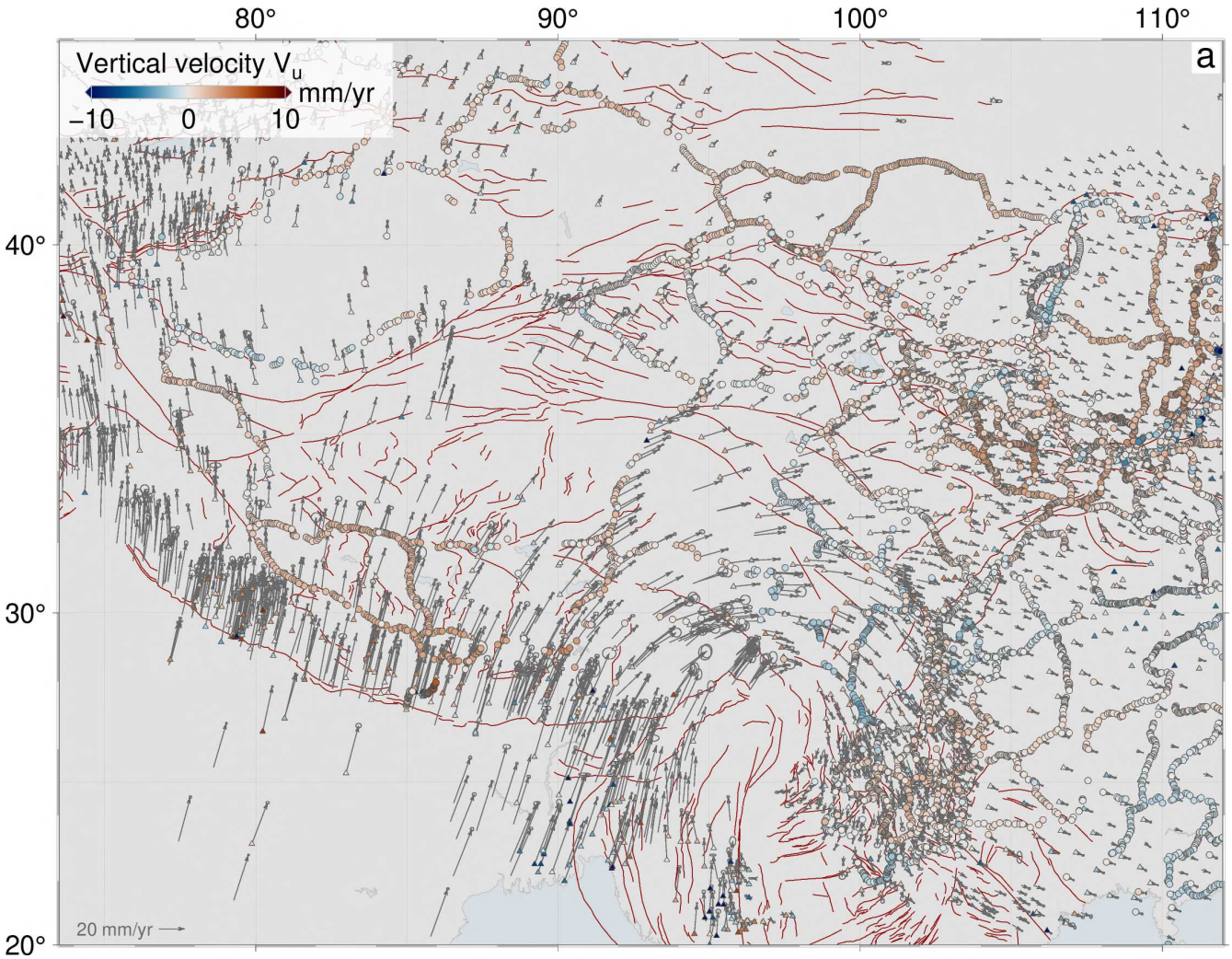

Fig. S2

Compilation of GNSS and levelling velocities in the study region (available at *66*), rotated into the Eurasia reference frame defined by *(76)*. Vectors show horizontal motion. Colors show vertical velocities, with constraints from GNSS shown as triangles and levelling measurements as circles (red is uplift).

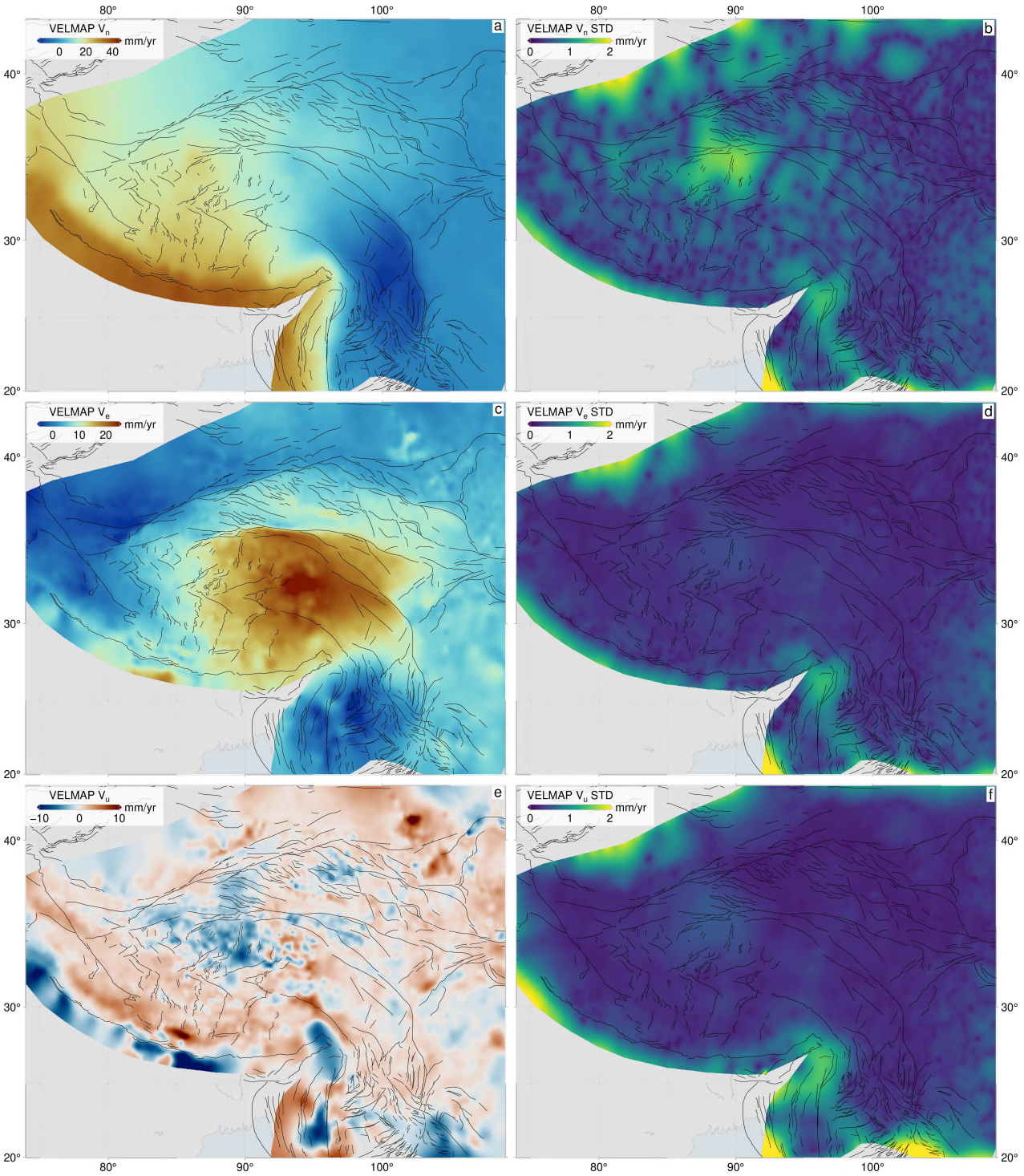

Fig. S3

The 3D *coarse* velocity model, obtained by joint inversion of InSAR and GNSS data to give velocities on the nodes of the triangular mesh (Fig. S1). (a) Northward velocity (positive values are towards north), (c) Eastward velocity (positive values are towards east), (e) Vertical velocity (positive values are uplift). Black lines show active faults from the Global Earthquake Model (*65*). The right column shows the spatial distribution of uncertainties (1 standard deviation) of the (b) northward, (d) eastward, and (f) vertical velocity components of the velocity field.

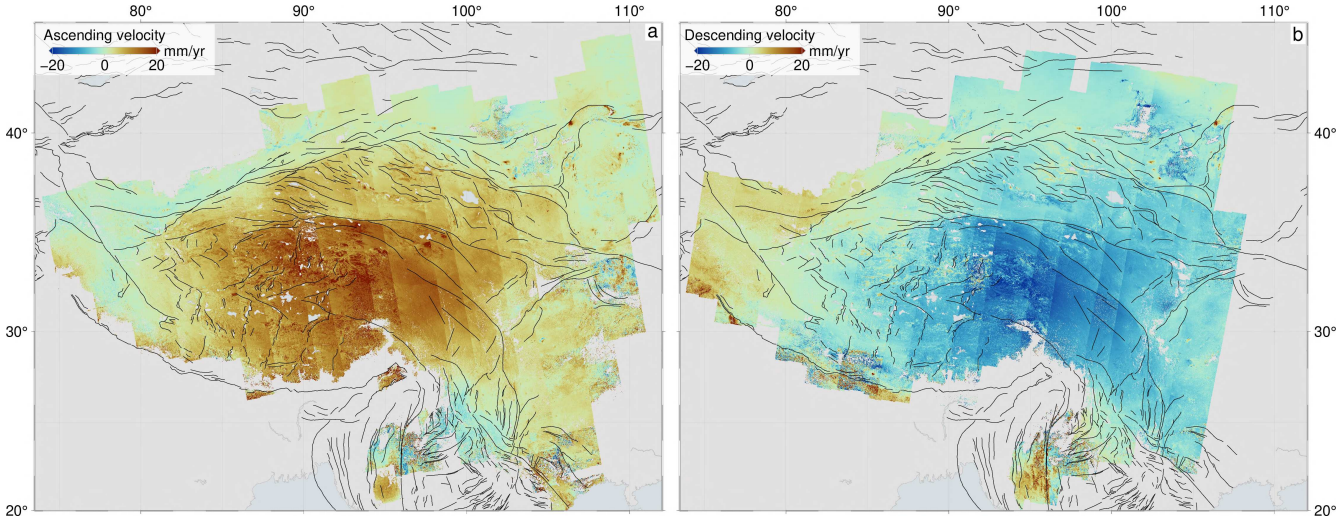

Fig. S4

Line-of-Sight (LOS) velocity mosaics in (a) ascending and (b) descending geometries for study area in a Eurasian Reference frame defined by GNSS. Positive indicates motion away from the satellite.

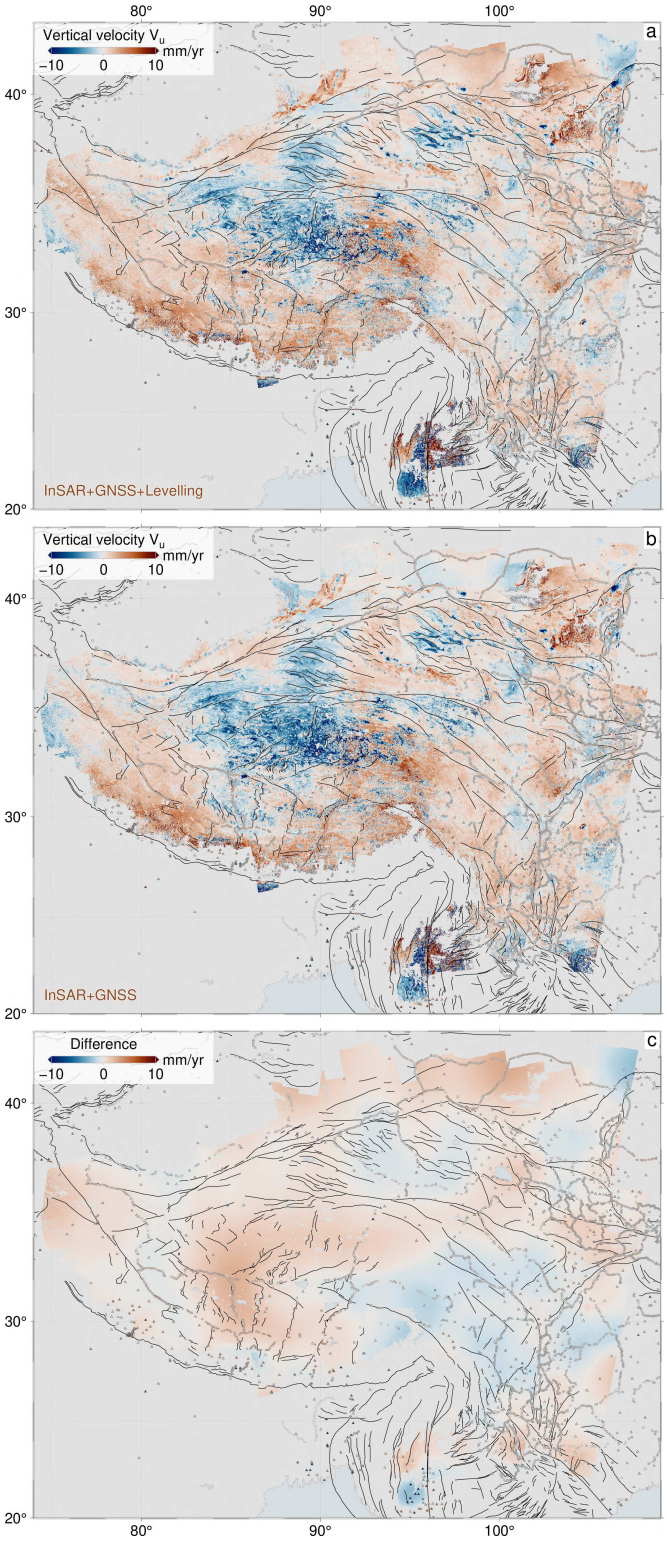

Fig. S5

Vertical velocity field for the Tibetan plateau at 1 km resolution, derived from combination of ascending and descending InSAR data shown in Fig. S4. (a) Vertical velocity field derived from inversion using vertical GNSS (colored triangles) and levelling (circles) data as constraints. (b) Vertical velocity field derived from inversion without using levelling data. (c) Difference between (a) and (b).

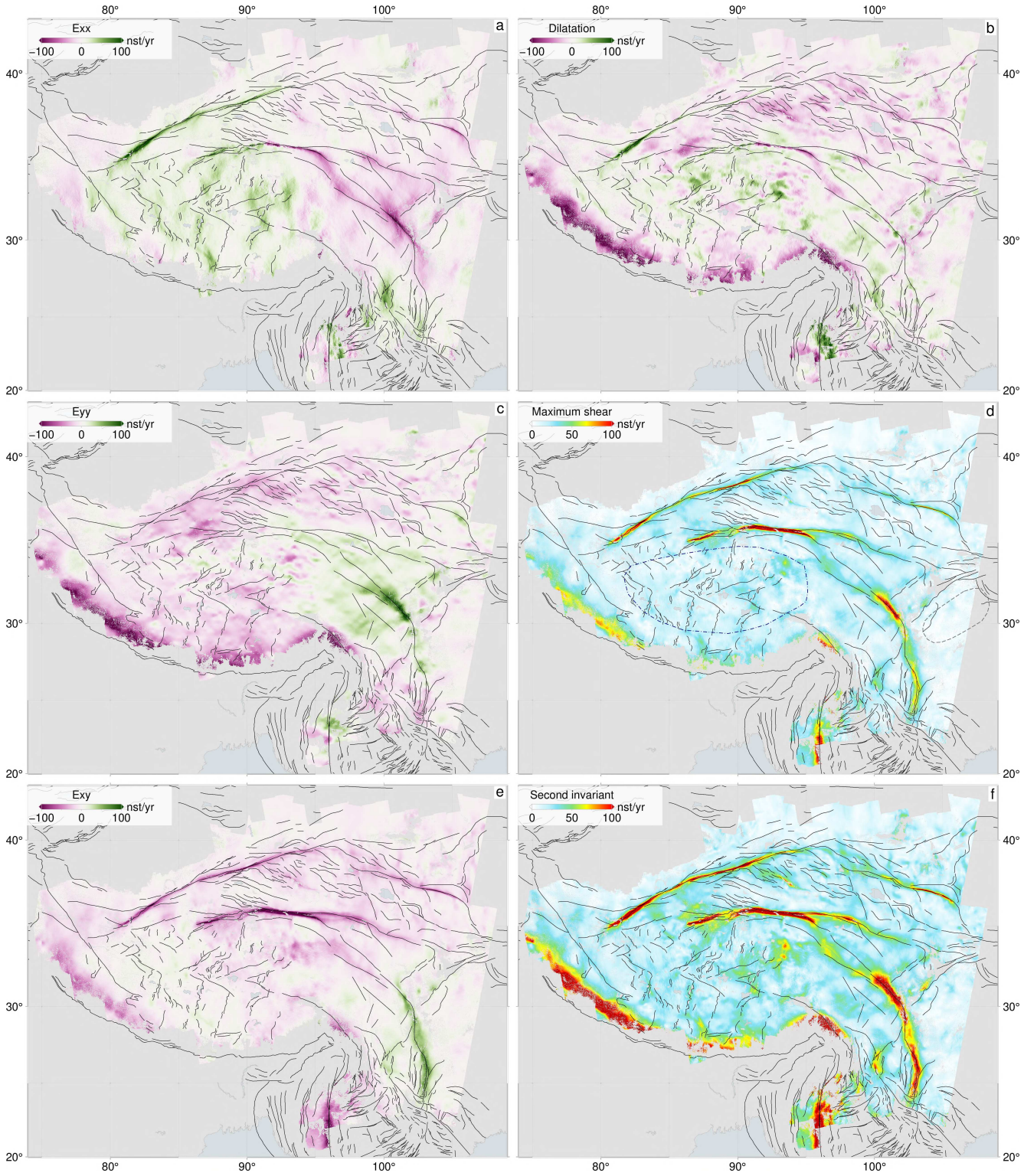

Fig. S6

Components of the horizontal strain rate tensor derived from the gradients of InSAR eastward and interpolated GNSS northward (Fig. S3a) velocities. Inset on each panel gives the component and color scale.

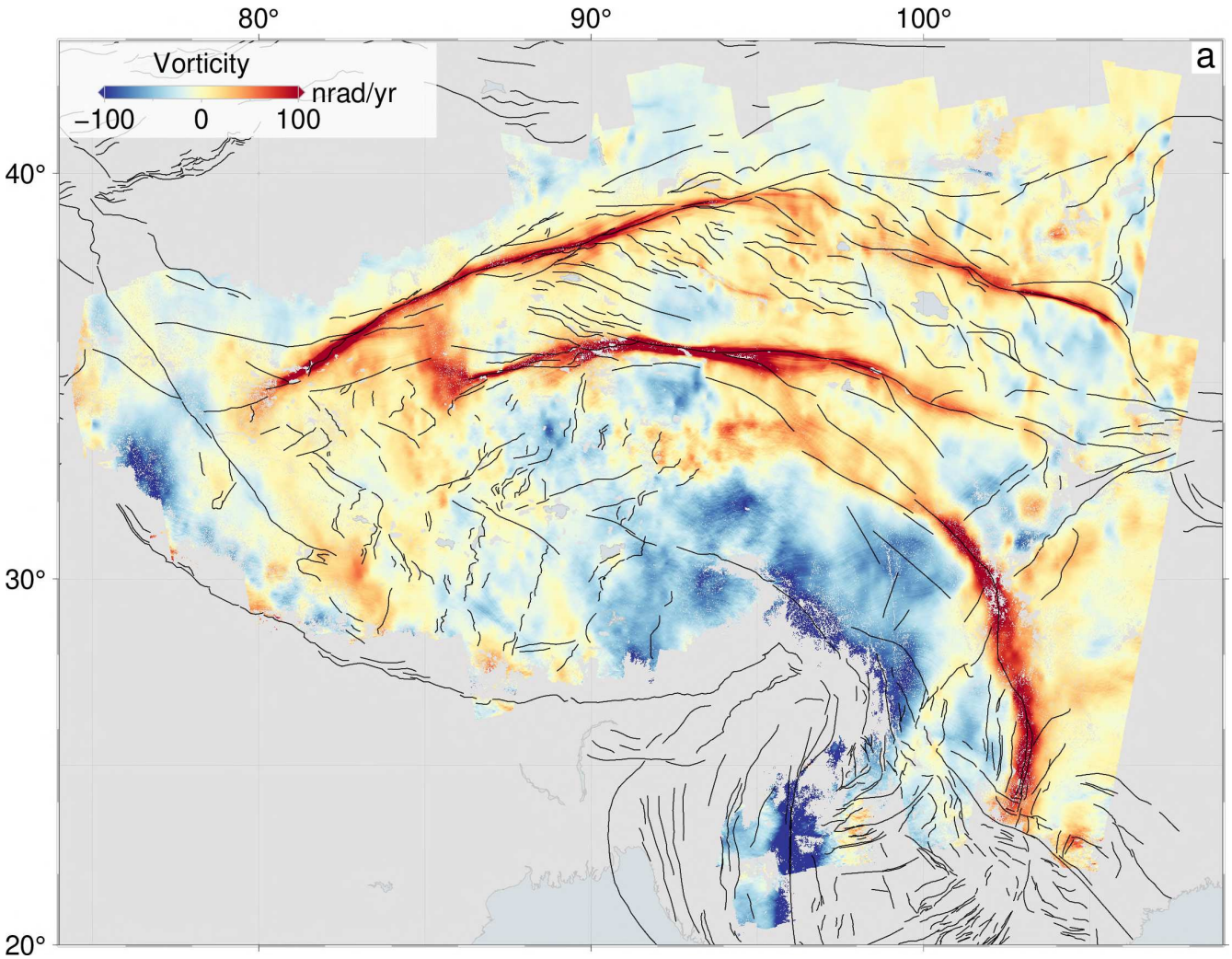

Fig. S7

Vorticity, with positive values indicating anti-clockwise rotation.

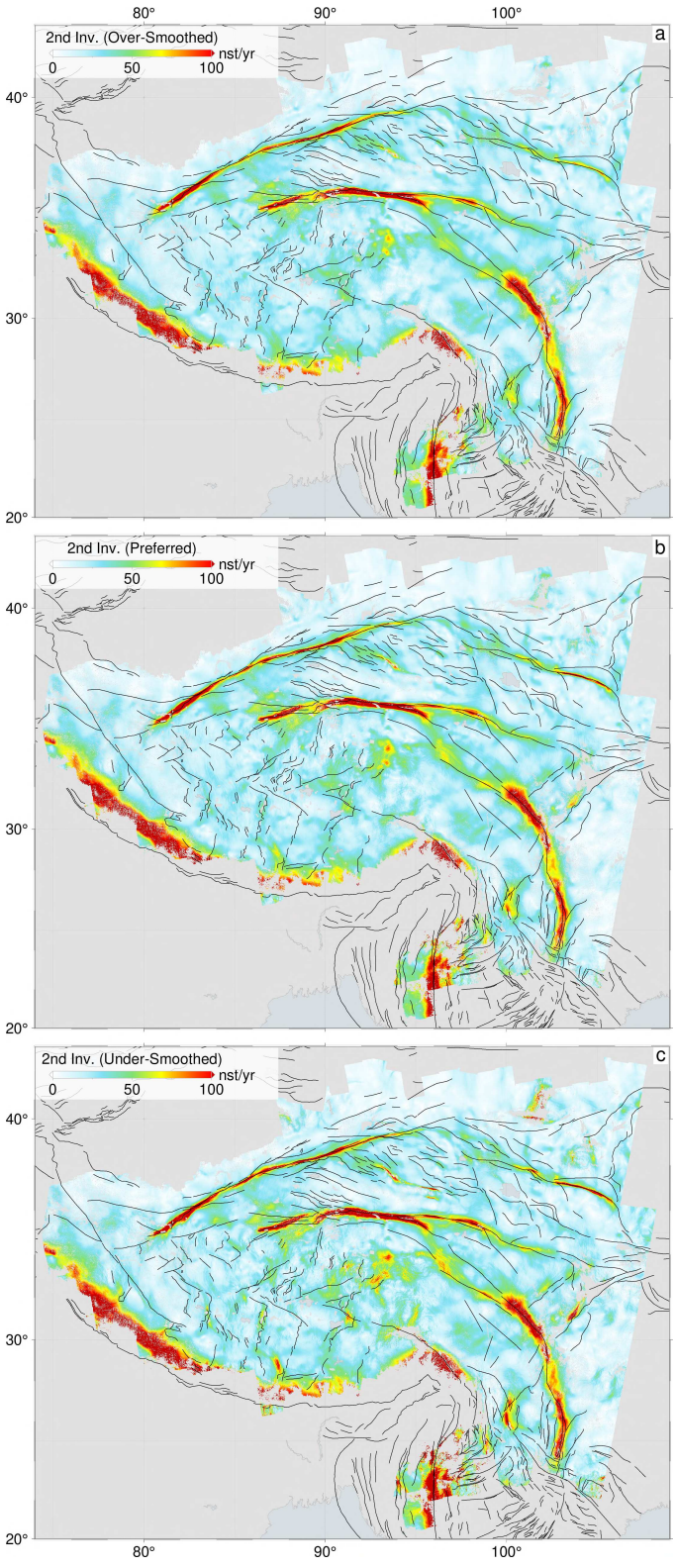

441

442 **Fig. S8**

443 Second invariant strain rate fields using different smoothing parameters for the east-west velocities. (a)
444 uses a median filtering window size of 200 km and is over-smoothed. (b) uses a window size of 150 km
445 and is our preferred solution. (c) uses a window size of 100 km and is under-smoothed.

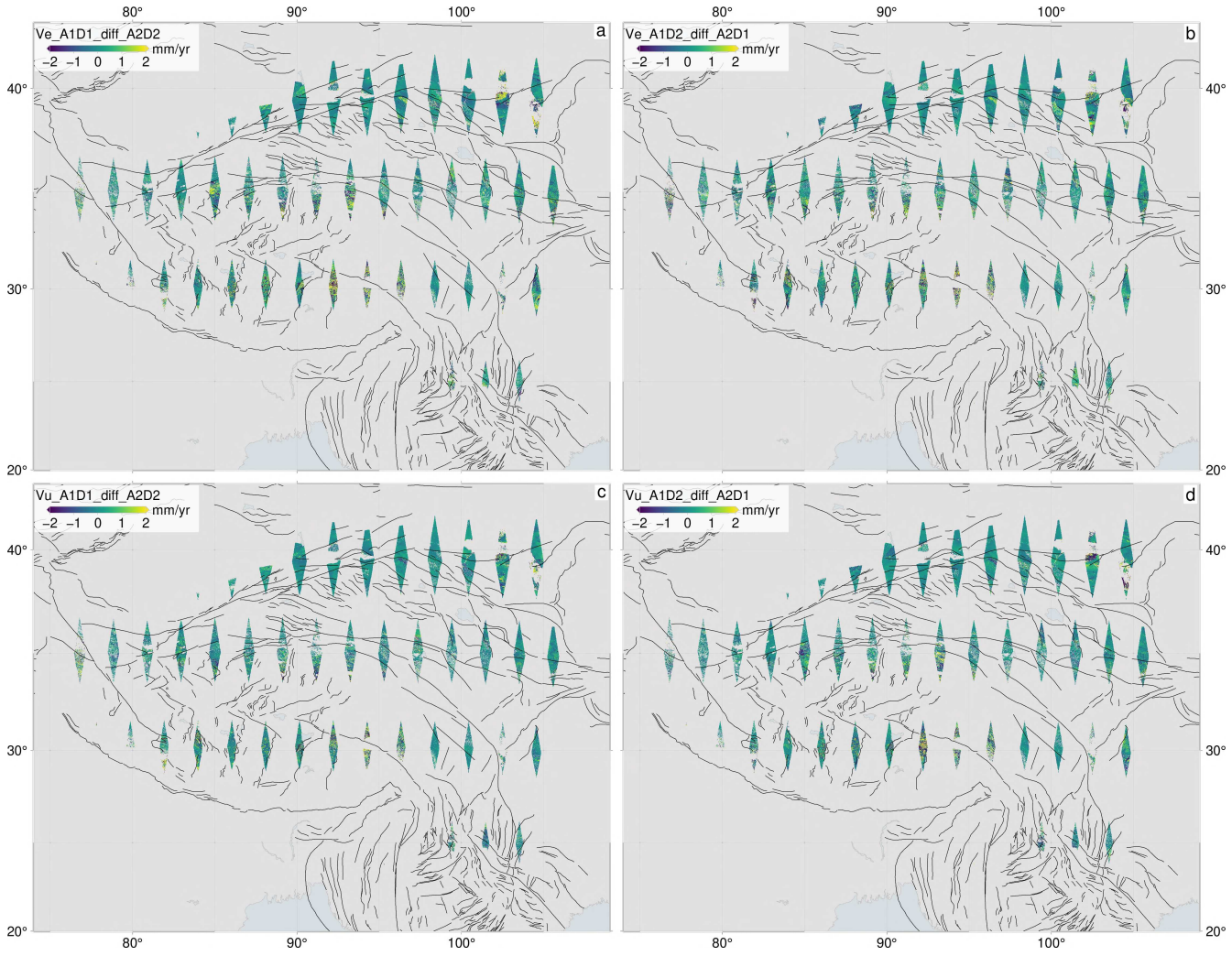

Fig. S9

Difference maps between independent estimates of east-west and vertical velocities, for pixels where 4 independent observations (2 ascending and 2 descending) exist.

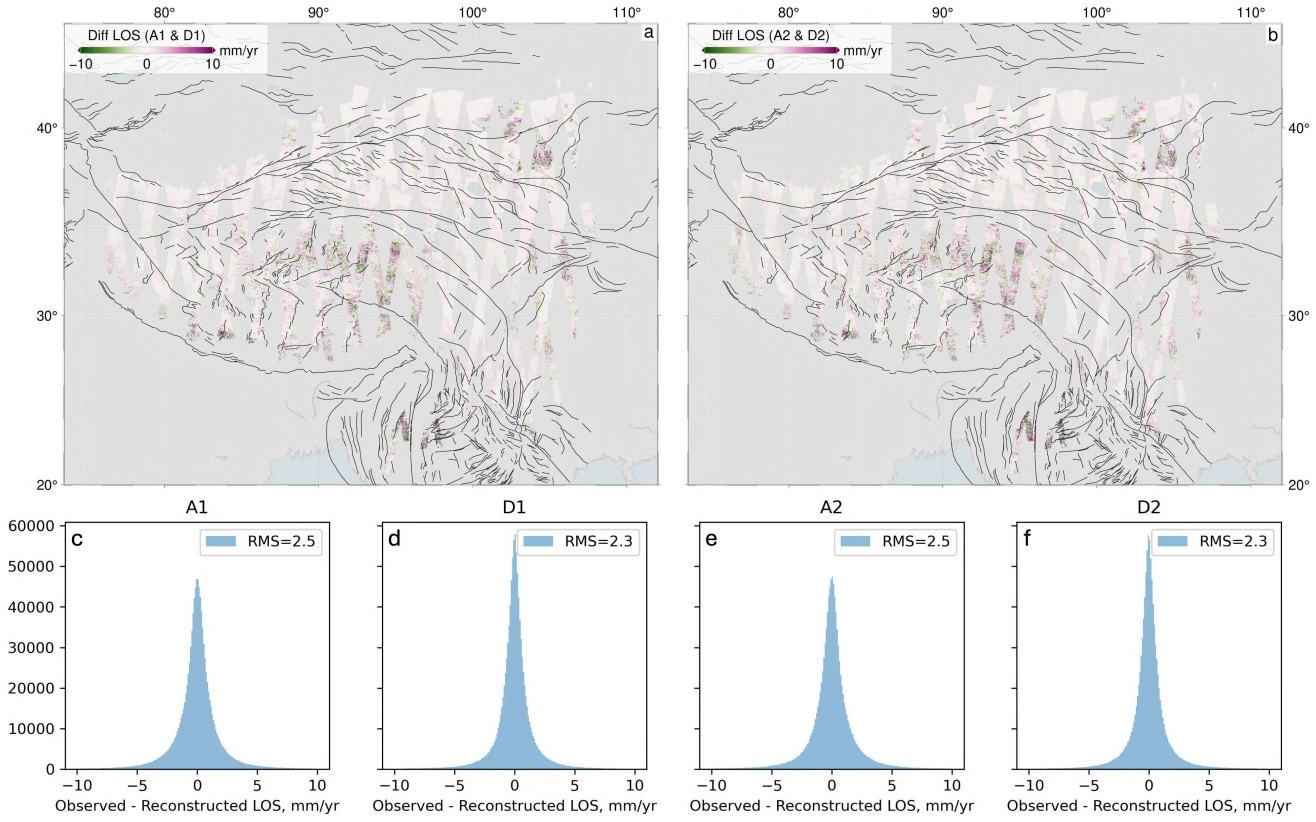

Fig. S10

LOS uncertainty analysis assessed by comparing observed and reconstructed LOS velocities at track overlaps. The observed LOS velocity field shown in Fig. S4 is divided into four non-overlapping groups of ascending and descending tracks: A1, A2, D1, and D2. (a–b) A1 represents the differences between the observed LOS velocities in A1 and the reconstructed LOS velocities at A1's pixel locations, derived using the LOS velocities from A2, D1, and D2. The same reconstruction approach is applied for D1, A2, and D2, respectively. (c–f) Residuals and root-mean-square (RMS) differences between the observed and reconstructed LOS velocities for each corresponding track group.

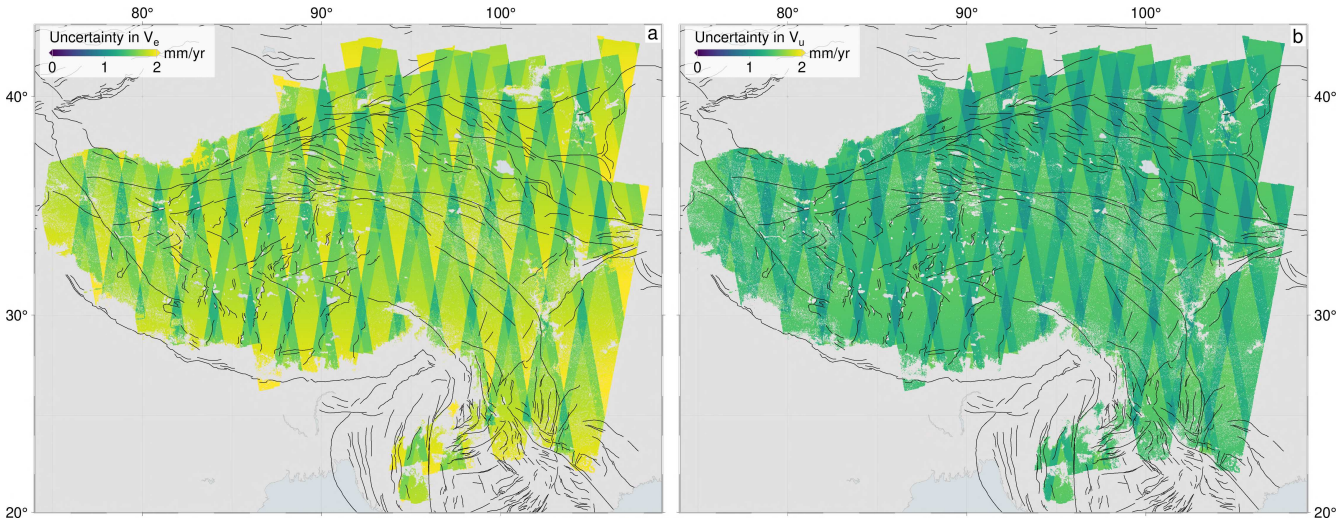

Fig. S11

Estimates of uncertainty (1σ) for 1 km grids of (a) east (V_e) and (b) vertical (V_u) velocities.

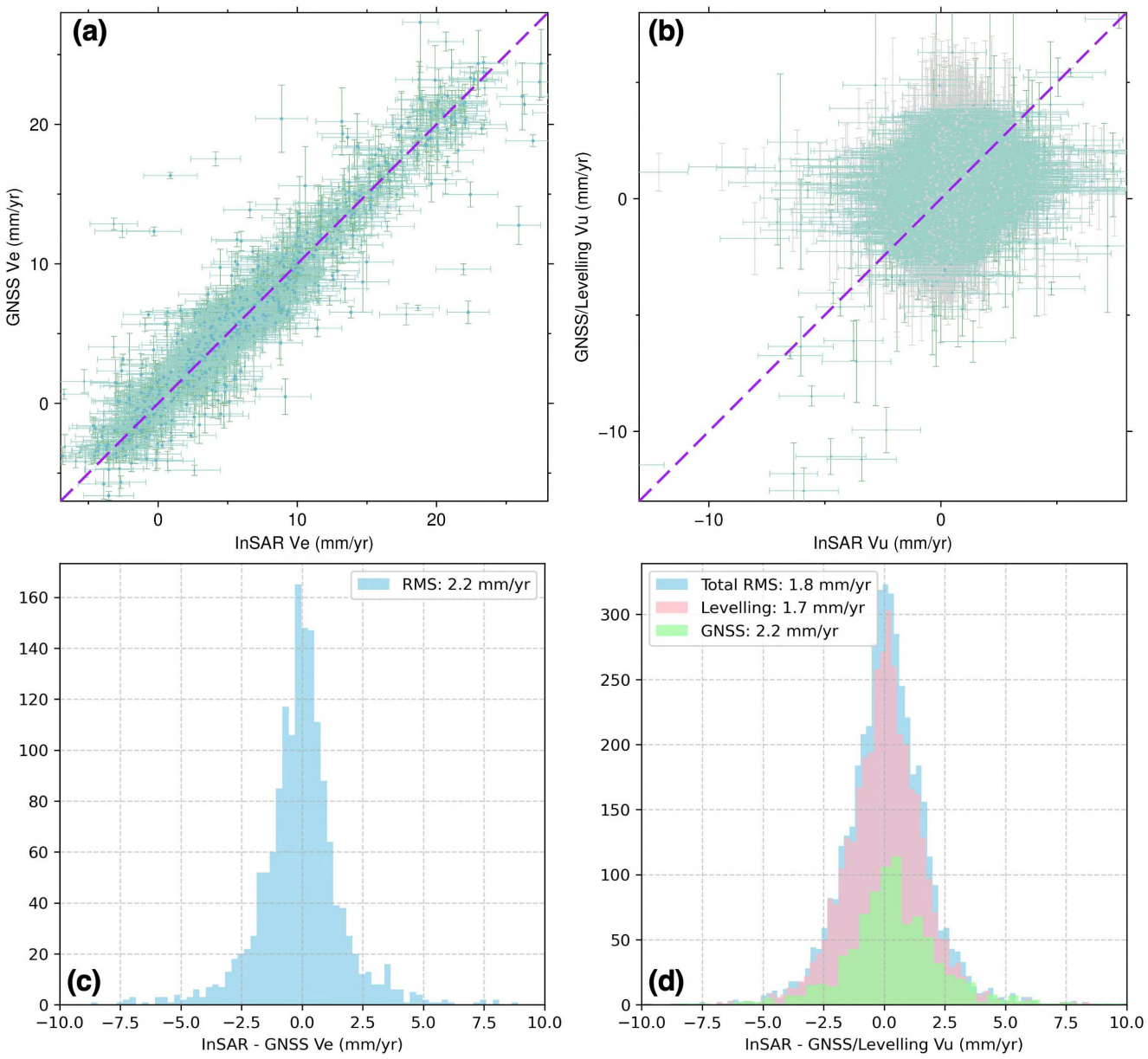

Fig. S12

Correlation plot of InSAR-derived (a) V_e and (b) V_u against (a) GNSS V_e and (b) GNSS/levelling V_u. Levelling data are denoted by gray bars. Purple dashed lines are one-to-one line for reference. The corresponding histograms of mismatch are shown in panels (c)-(d).

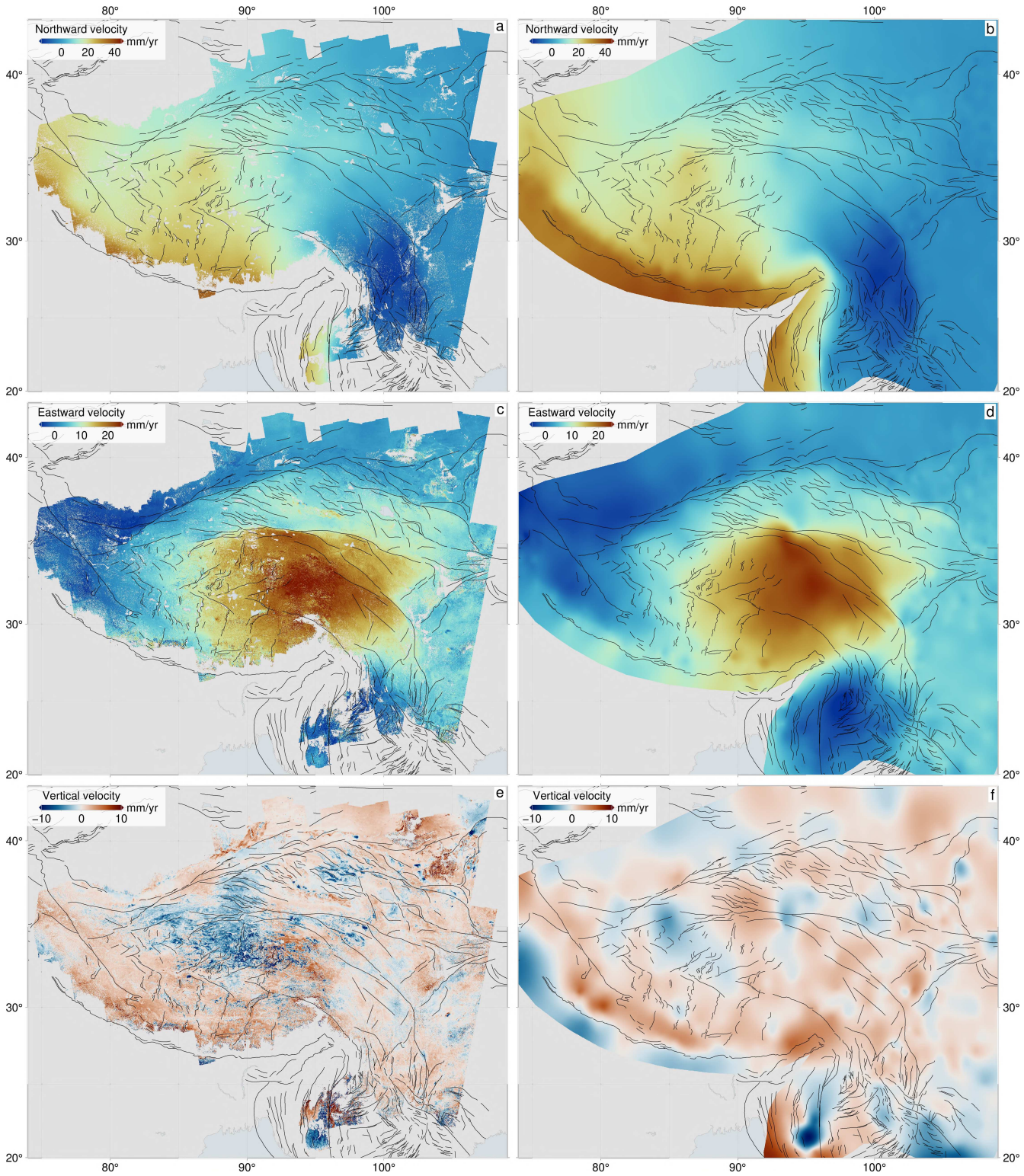

Fig. S13

(a, c, e) 3D velocities derived through the inclusion of InSAR data, and (b, d, f) velocities constrained by GNSS and levelling observations only. Inset in each panel indicates the component and color scale.

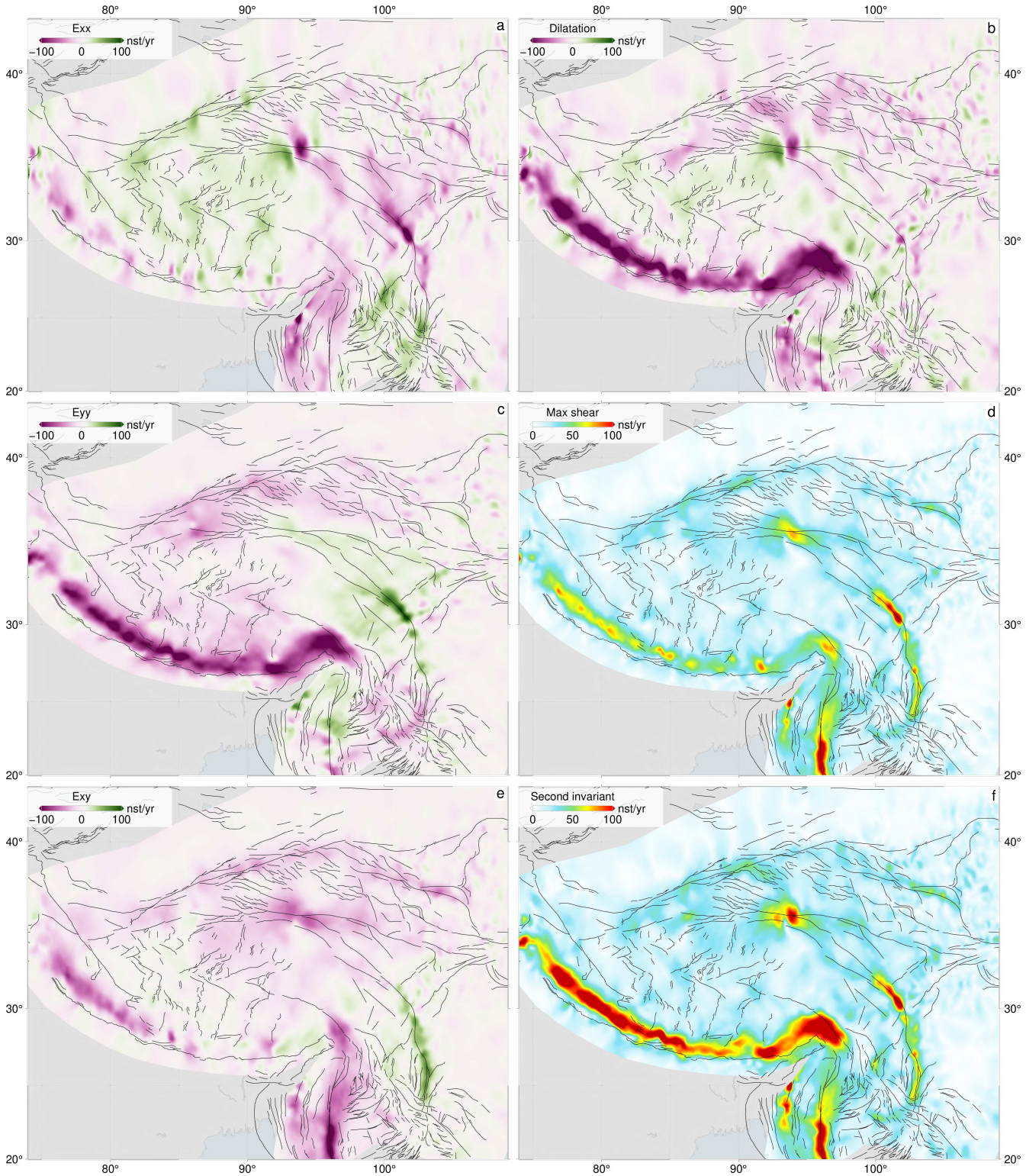

Fig. S14

Components of the horizontal strain rate tensor derived from the gradients of interpolated GNSS horizontal velocities (Fig. S13b,d). See Fig. S6 for comparison with results obtained through the inclusion of InSAR data.

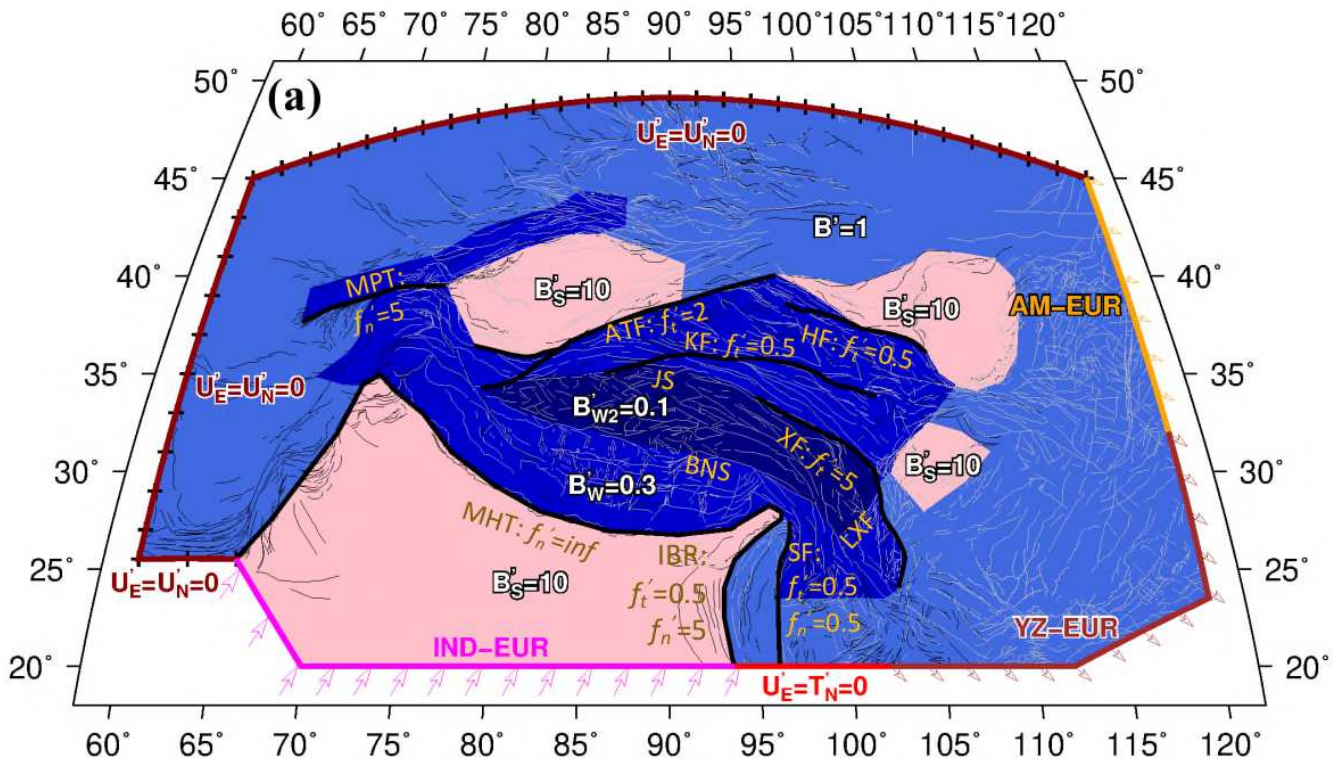

Fig. S15

Boundary and internal conditions for the dynamic faulted thin viscous shell model after (*10*). The maroon outer boundary with black tick marks is held fixed with zero velocity, where the other boundaries are given velocities imposed by far-field plate motion poles of rotation for the Indian (IND), Yangtze (YZ), and Amur (AM) plates relative to Eurasia (EUR), except for the small region east of India marked in red, where the eastward velocities and northward tractions are set to zero. Colors mark regions with different dimensionless viscosity coefficient, labeled as *B'*, relative to background far-field values *B'* = 1; pink areas are strong, and dark blue areas are weaker than average. Thick black lines are the faults that are allowed to slip in this model with values of the dimensionless fault-resistance coefficient *f'* on each fault determined by systematic comparison of model velocity field with observed geodetic velocity sampled from Fig. S3. Viscous flow equations were solved using the 2D finite-element code, *basil* (*10,43*). Details of how parameters are made dimensionless are given in *(10)*. Model faults: ATF, Altyn Tagh Fault; HF, Haiyuan Fault; IBR, Indo-Burma Ranges; KF, Kunlun Fault; MHT, Main Himalayan Thrust; MPT, Main Pamir Thrust; SF, Sagaing Fault; XF, Xianshuihe Fault.

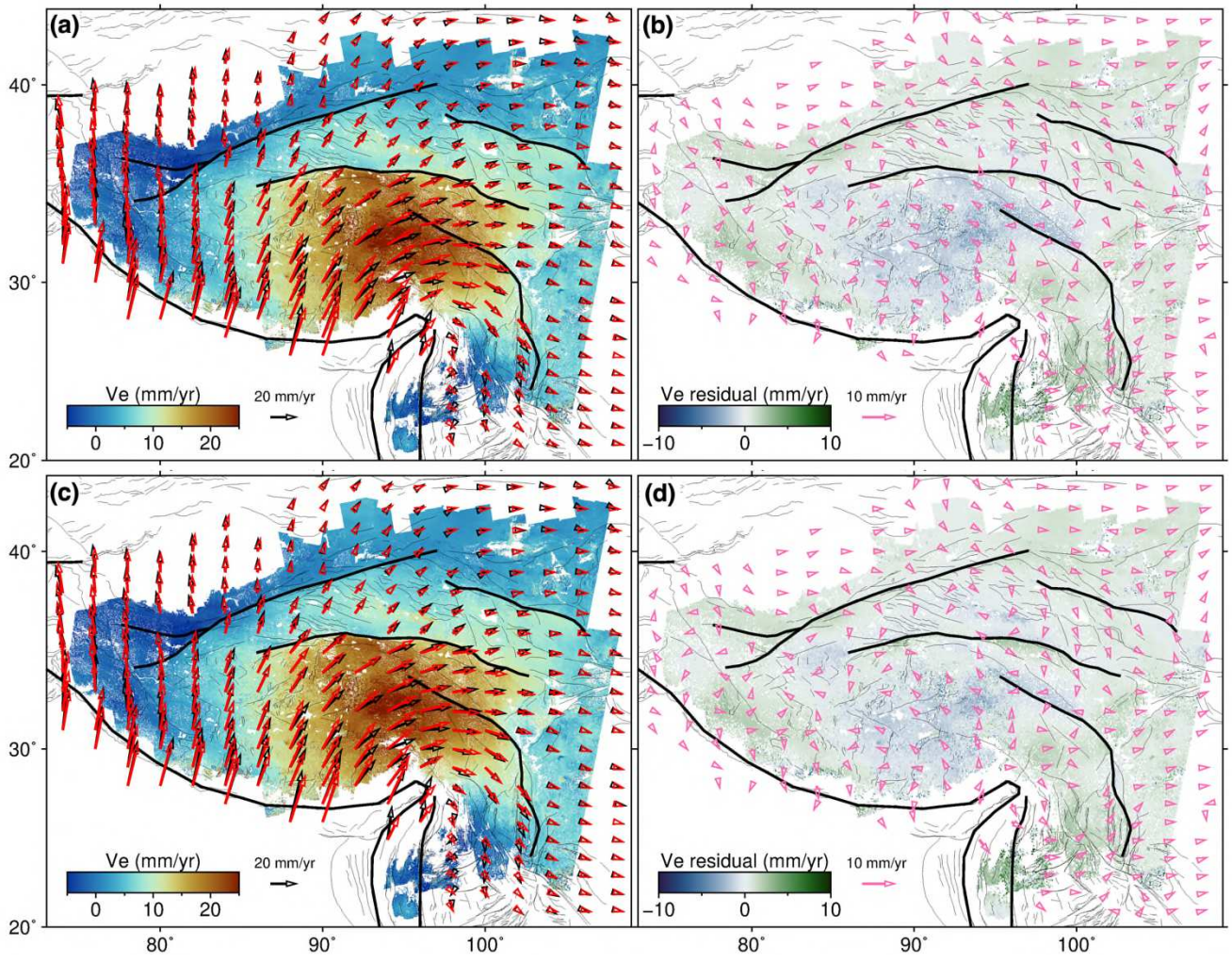

Fig. S16

Observations, dynamic model predictions, and residuals for horizontal velocities. (a, c) Eastward velocities (Ve), overlaid with observed (black, sampled from Fig. S3a,b) and modelled (red) velocity vectors. (b, d) Residual Ve field, with residual velocity vectors shown as pink arrows. (a, b) show results for our preferred model with f'=0.5 applied to the Kunlun Fault, while (c, d) show results for a test model with f=0 on the Kunlun Fault.

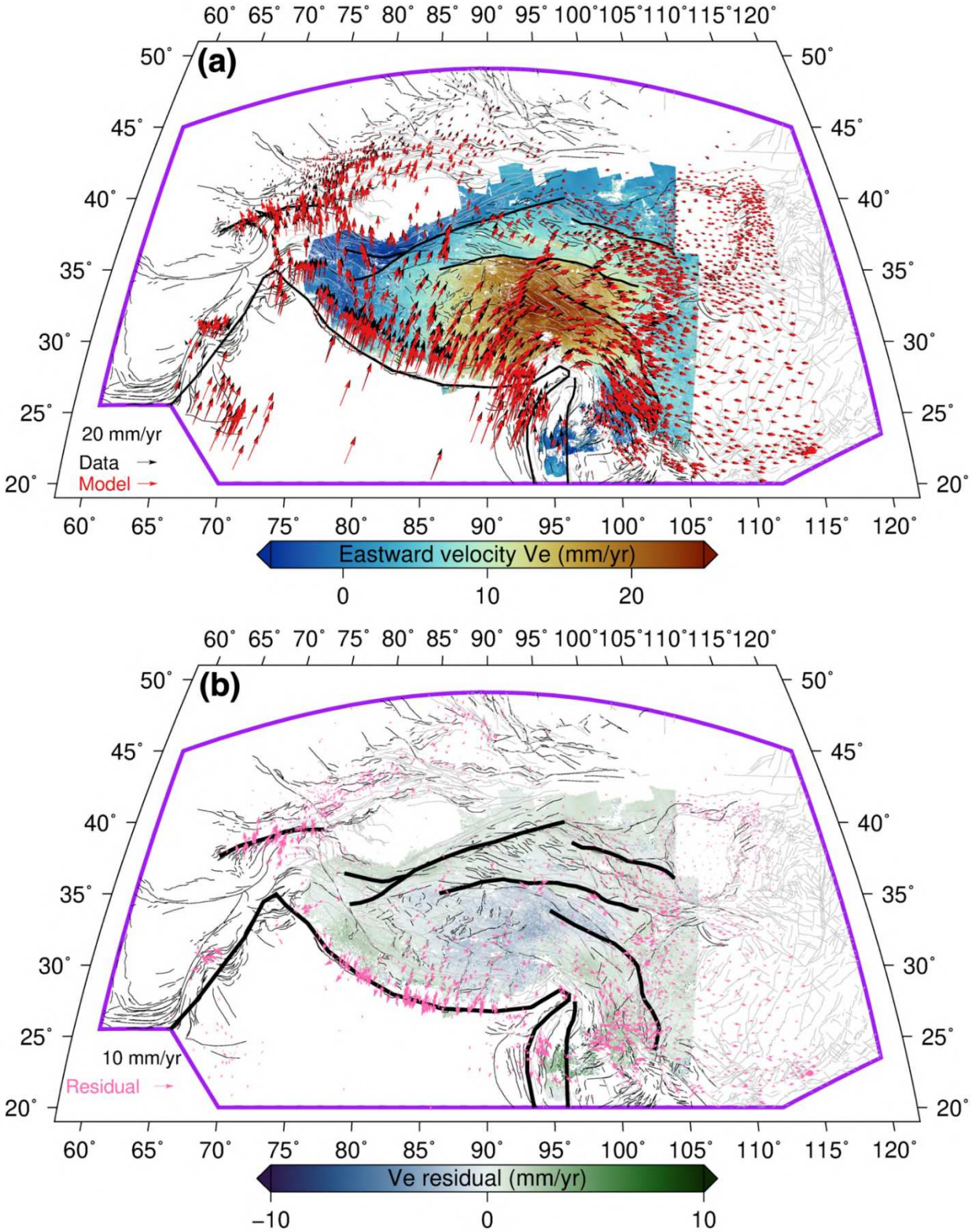

Fig. S17

Same as Fig. S16a,b, but overlaid with observed and modelled GNSS horizontal velocities (a) and residuals (b).

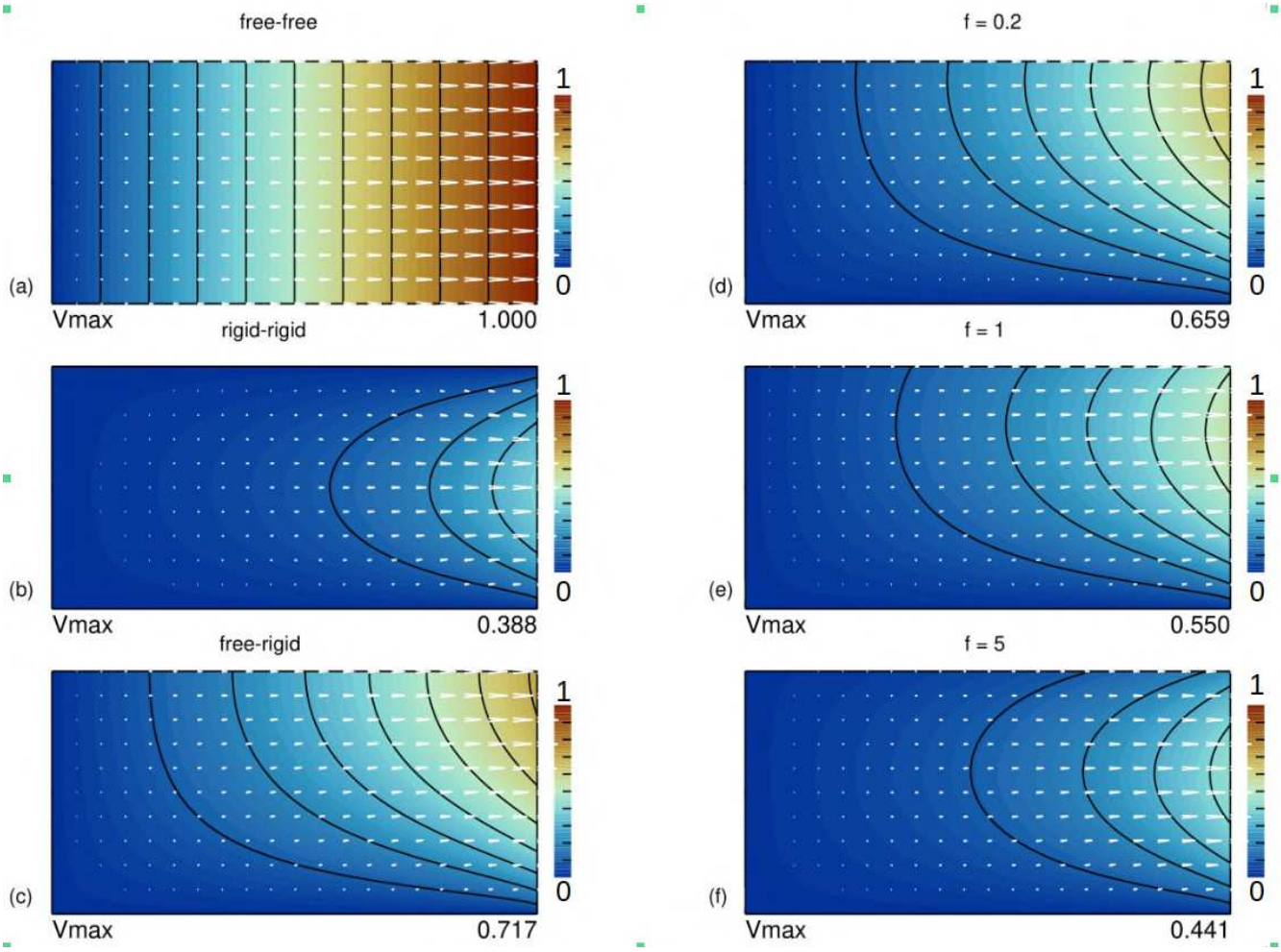

Fig. S18

Maps of the x-component of velocity in the domain $0 \leq x \leq S = 2$ and $0 \leq y \leq W = 1$ for different boundary conditions in the case of $n = 1$ and uniform viscosity. In all cases the y-component of velocity is zero on all 4 boundaries, the x=0 boundary is rigid, and the x=S boundary has an applied outward normal traction $\sigma_T = 1$ that is constant in y. For all except (a) the boundary y=0 is free. The two horizontal boundaries are zero shear-stress for (a) and zero velocity for (b). The boundary y=W is zero stress for (c), and (d-f) use fault resistance coefficient $f' = 0.2$ (d), 1 (e) and 5 (f). The maximum velocity in each panel (Vmax) is indicated by the number in the bottom right.

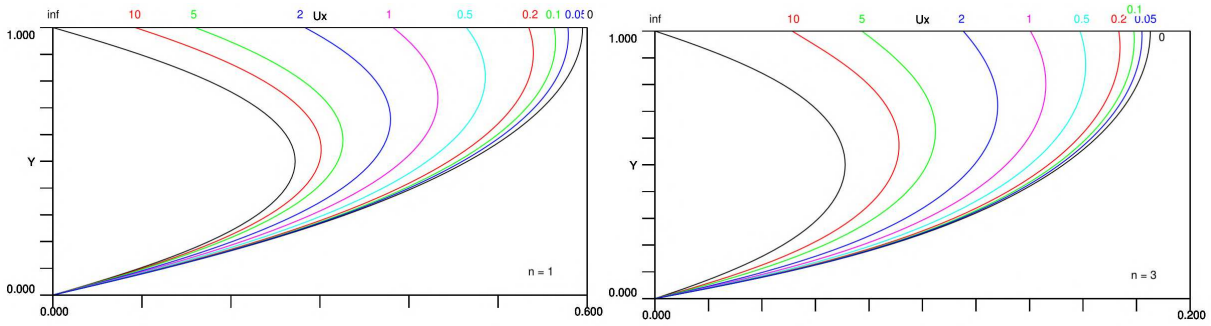

Fig. S19

Profiles of the *x*-component of velocity along the line $x = 1.75$ for (left) constant viscosity (as Fig. S18*b-f*) and (right) for similar calculations using power-law flow with $n = 3$. The value of *f'* applied to the north boundary is indicated for each profile.

References:

(The following references only appear in the supplement. References 1-66 are listed in the main manuscript)

67. T. Wright, B. Parsons, Z. Lu, Toward mapping surface deformation in three dimensions using InSAR. *Geophys. Res. Lett.* **31** (2004)

68. P. England, G.A. Houseman, L.Sonder, Length scales for continental deformation in convergent, divergent, and strike-slip environments: Analytic and approximate solutions for a thin viscous sheet model, *J. Geophys. Res. Solid Earth* **90**, 3551-3557 (1985).

69. Yu, C., Li, Z., Penna, N. T., Crippa, P., Generic atmospheric correction model for interferometric synthetic aperture radar observations, *J. Geophys. Res. Solid Earth* **123**(10), 9202-9222 (2018).

70. Z. Yunjun, Fattahi, H., Pi, X., Rosen, P., Simons, M., Agram, P., Aoki, Y., Range geolocation accuracy of C-/L-band SAR and its implications for operational stack coregistration. *IEEE Trans. Geosci. Remote Sens.* **60**, 1-19 (2022).

71. X. Xu, Sandwell, D. T., Toward absolute phase change recovery with InSAR: Correcting for earth tides and phase unwrapping ambiguities. *IEEE Trans. Geosci. Remote Sens.* **58**(1), 726-733 (2019).

72. P. Wessel, Luis, J. F., Uieda, L. A., Scharroo, R., Wobbe, F., Smith, W. H., Tian, D., The generic mapping tools version 6. *Geochem. Geophys. Geosyst.* **20**(11), 5556-5564 (2019).

73. M. Lazecky, Fang, J., Hooper, A., Wright, T., Improved phase unwrapping algorithm based on standard methods. In *IGARSS 2022-2022 IEEE International Geoscience and Remote Sensing Symposium* (pp. 743-746). IEEE (2022).

74. O. L. Stephenson, *et al.*, The impact of plate motions on long-wavelength InSAR-derived velocity fields. *Geophys. Res. Lett.* **49**(21), e2022GL099835 (2022).

75. J. Elliott *et al*., Deformation, Strains and Velocities for the Alpine Himalayan Belt from trans-continental Sentinel-1 InSAR & GNSS. EarthArXiv eprints (2025): https://doi.org/10.31223/X5GX6B.

76. Z. Altamimi, *et al.*, ITRF2014 plate motion model. *Geophys. J. Int.* **209**, 1906–1912 (2017).

77. A. Love, A treatise on the mathematical theory of elasticity. Courier Corporation, (1944).

78. J. Fang *et al*., Strain partitioning in the Southeastern Tibetan Plateau from kinematic modeling of high-resolution Sentinel-1 InSAR and GNSS. Geophysical Research Letters, **51**(19), 2024GL111199 (2024).